Structure of active human telomerase with telomere shelterin protein TPP1

Baocheng Liu[1,4], Yao He[1,2,4], Yaqiang Wang[1], He Song[1], Z. Hong Zhou[2,3], and Juli Feigon[1]*

1 Department of Chemistry and Biochemistry, University of California, Los Angeles; Los Angeles, CA 90095-1569, USA

2 Department of Microbiology, Immunology, and Molecular Genetics, University of California, Los Angeles; Los Angeles, CA 90095, USA

3 California NanoSystems Institute, University of California, Los Angeles; Los Angeles, CA 90095, USA

4 These authors contributed equally to this work

*Corresponding author. Email: feigon@mbi.ucla.edu

Human telomerase is an RNA-protein complex that extends the 3′-end of linear chromosomes by synthesis of multiple copies of the telomeric repeat TTAGGG[1]. Its activity is a determinant of cancer progression, stem cell renewal, and cellular aging[2-5]. Telomerase is recruited to telomeres and activated for telomere repeat synthesis by the telomere shelterin protein TPP1[6,7]. Human telomerase has a bilobal structure with a catalytic core RNP and an H/ACA RNP[8,9]. Here we report cryo-EM structures of human telomerase catalytic core of telomerase reverse transcriptase (TERT) and telomerase RNA (TER or hTR) at 3.3Å and the first structure with the shelterin protein TPP1, at 3.5Å resolution. TPP1 forms a structured interface with the TERT-unique TEN and TRAP domains and conformational dynamics of TEN–TRAP are damped upon TPP1 binding, defining the requirements for recruitment and activation. The structures further reveal that elements of TERT and TER involved in template and telomeric DNA handling, including TEN domain and TRAP–thumb helix channel, are largely structurally homologous to those in Tetrahymena telomerase[10], and provide unique insights into mechanism. The binding site of telomerase inhibitor BIBR1532[11,12] overlaps a critical interaction between TER pseudoknot and TERT thumb domain. Numerous mutations leading to telomeropathies[13,14] are located at the TERT–TER and TEN–TRAP–TPP1 interfaces, highlighting the importance of TER–TERT and TPP1 interactions for telomerase activity, recruitment, and as drug targets.

MAIN

Telomerase is a reverse transcriptase that uniquely forms an RNP with a rapidly-evolving non-coding telomerase RNA, that is required for activity, localization, and assembly with TERT and other species-specific proteins[15,16]. Telomerase is usually only active in stem cells and germ line cells; its absence in somatic cells limits their proliferative lifespan due to shortening of telomeres beyond a critical length[5]. Telomerase reactivation in most cancer cells is essential for their immortal phenotype[3,4], while many telomere biology disorders, including various cancers, are a consequence of specific mutations in telomerase components[17]. Among these, TERT is the most frequently mutated, followed by TER[18,19]. Cryo-EM structures of human and *Tetrahymena* telomerase have defined the holoenzyme architectures, components, and interactions and provided insights into mechanism[8-10,20,21]. However, an understanding of the structural basis of diseases of telomerase insufficiency and development of drugs to inhibit or restore telomerase activity—a long standing goal to treat premature aging and cancer—has been hindered by lack of detailed knowledge of atomic level interactions in human telomerase TERT–TER catalytic core and with TPP1.

TPP1 is one of six shelterin proteins (TPP1, POT1, TRF1, TRF2, RAP1, TIN2) that associate in various complexes with the telomeric DNA[7,22]. TPP1 plays a critical role in regulation of telomere length, as it both recruits and activates telomerase[6]. TPP1 interacts directly with POT1, which binds the single-stranded telomeric DNA 3′-overhang, and with TIN2, which simultaneously binds TRF1 and TRF2 dimers that interact with the double-stranded DNA[22]. TPP1–POT1 switches from telomerase inhibitory by sequestering the 3'-end of telomeric DNA on POT1, to highly activating when TPP1 is bound to telomerase[6,23]. Biochemistry and genetic studies in cells have shown that TPP1 OB domain interacts with TERT through a glutamate (E) and leucine (L)-rich patch (TEL-patch) and the N-terminus of its OB domain (NOB)[24-27]. POT1 binds TPP1 on a POT1-binding domain separated by a linker following OB[28,29] (Fig. 1a). High resolution cryo-EM structures of *Tetrahymena* telomerase established that p50, a constitutive component that is an ortholog of the activating functions of TPP1, binds TERT-

unique telomerase essential N-terminal domain (TEN) and telomerase RAP motif (TRAP)[10,20]. However, TPP1 only transiently interacts with human telomerase in a cell cycle-dependent manner[30], making structural studies challenging. Here we purified human telomerase in complex with TPP1 and telomeric DNA and determined their cryo-EM structures. These structures define the determinants of telomerase recruitment to telomeres by TPP1, reveal the unique TERT–TER interactions that regulate telomerase activity, assembly, and template–DNA handling, and localize numerous mutations at these interfaces that lead to diseases of telomerase insufficiency.

Overall structure

Human telomerase with DNA primer d(T_{12}TTAGGG) was affinity purified in three steps as described in Methods. The purified DNA-bound telomerase was incubated with ~10-fold excess of TPP1 OB domain (hereafter referred as TPP1) (Fig. 1a) prior to vitrification on cryo-EM grids. As previously described[8,9], telomerase has a bipartite structure with a catalytic core RNP (Fig. 1b-d) and H/ACA RNP (Fig. 1f,g) flexibly connected by P1a and P4.1-P4.2-P5 regions of TER (Fig. 1e). Separate focused refinements of the two RNPs gave resolutions of 3.3–3.8 Å for TERT–TER catalytic core and 3.2 Å for H/ACA RNP (Fig. 1b,c,f, Extended Data Fig. 1-3). The telomerase H/ACA RNP has a non-canonical function in telomerase biogenesis and localization, rather than pseudouridylation of specific substrates[31]. The H/ACA RNP comprises two complete sets of H/ACA proteins Dyskerin, GAR1, NOP10, and NHP2 bound to successive irregular stem-loops (P4 and P7) followed by box H (AGAGGAA) and box ACA nucleotides, respectively, and a single TCAB1 bound at P8 apical loop with Dyskerin and NHP2 (Fig. 1e-g, Extended Data Fig. 4a). The H/ACA RNP model is almost the same as reported[8] and is not discussed further here.

The catalytic core comprises TERT and TER template/pseudoknot (t/PK) and conserved region 4-5 (CR4/5)[32]. TERT has conserved RNA-binding domain (RBD), reverse transcriptase (RT), and C-terminal extension (CTE) that form a ring, while the TERT-unique TEN and TRAP (a large insertion in RT fingers) form a complex above the TERT ring[10,20] (Fig. 1a,b, Extended

Data Fig. 5a,b). TPP1 binds to TERT TEN and TRAP (Fig. 1a,c,d). CR4/5 extends from P4, with P5, P6, and P6.1 connected by a three-way junction (Fig. 1e, Extended Data Fig. 4a). About 22% of particles also contain density corresponding to the histone H2A/H2B dimer previously observed at somewhat higher percentage, bound at and possibly stabilizing this three-way junction[8] (Fig. 1d, Extended Data Fig. 3a,b). The overall higher resolution of the catalytic core in the present study allowed us to assign sequence more accurately to cryo-EM density and position side chains (Fig. 1d, Extended Data Fig. 2).

TPP1 interactions with TEN–TRAP

A notable difference between the catalytic core without[8] and with TPP1 is the higher resolution of the density for TEN (Fig. 2a). This allowed us to accurately model TEN, where previous modeling[8] had ~1/3 of the residues in the wrong register. The overall structures of human TEN and TRAP, as well as the extended β-sheet between TEN and TRAP, are remarkably similar to those in *Tetrahymena* telomerase (Fig. 2b, Extended Data Fig. 5b). However, the position of TEN–TRAP relative to the TERT ring is different, which may be caused by the double-stranded end of PK (P2a.1) abutting the TEN in human (Extended Data Fig. 5c-f). TRAP is connected at its N- and C-terminal ends to conserved helices IFD_A and IFD_C, respectively, by flexible linkers that allow positional dynamics of TEN–TRAP relative to the TERT ring (Fig. 2b).

The architecture of TPP1 bound to telomerase is the same as for the free protein[33], except at its interface with TEN–TRAP, where loop α2-β4 forms a short helix α2.1 (Fig. 2c). TPP1 loop α2-β4 and NOB[27] are shifted to positions similar to those in *Tetrahymena* telomerase-bound p50[10], but adopt different conformations (Extended Data Fig. 6a). Comparison of the cryo-EM density of TEN–TRAP in telomerase without and with TPP1 provides insight into conformational changes caused by TPP1 binding. TRAP is largely unchanged, while the TEN interface with TPP1 and TRAP becomes structured as evidenced by the stronger density, especially for its β3-β4, β4-α6 linker, and α7 (Extended Data Fig. 6i, j). Thus, TPP1 binding stabilizes the interaction between TEN and TRAP. TPP1 binding also damps the positional dynamics of TEN–TRAP as evidenced by the improvement in cryo-EM density on the outside surface of TEN (Fig. 2a,

Extended data Fig. 6i, j).

Superposition of TPP1–TEN–TRAP on *Tetrahymena* p50–TEN–TRAP[10] reveals that globally the binding interfaces are the same, including their three-way interaction[20] (Extended Data Fig. 6), but most specific interactions are not conserved (Supplementary Fig. 2). There is a continuous interface between TPP1 and TEN–TRAP (Fig. 2e, Extended Data Fig. 6e) that on TRAP includes interactions with residues previously identified as TEL patch[24] and NOB[27] (Fig. 2c). We identified three charge-charge interactions, TEN K78–TPP1 E215, previously identified by charge swap experiment[34], TRAP R774–TPP1 E168 (TEL patch) and TEN D129–TPP1 R92 (NOB) (Fig. 2d). The rest of the interface is primarily hydrophobic, involving mostly leucines on TRAP and TPP1 (Fig. 2f) and short side-chains (A, G, S) on TEN (Fig. 2e). Among these, TERT mutations R774L and Y772C are associated with dyskeratosis congenita and aplastic anemia, respectively[13]. Except for K78, most of the residue substitutions or disease mutations substitutions previously inferred to disrupt direct TPP1–TERT interactions[8,10,35,36] actually act indirectly, either by destabilizing the TEN–TRAP interface or changing TEN or TRAP structure (Extended Data Fig. 7a-c).

Alanine substitutions on TEN–TRAP interface residues were tested by telomerase direct activity assay to evaluate their importance in TPP1 binding (see methods). TPP1 enhanced telomerase activity ~twofold with only a small effect on repeat addition processivity (RAP)[24], similar to *Tetrahymena* p50[37], under optimized conditions of excess TPP1 . All mutants showed significant decreases of this activity stimulation, from ~50-85% (see methods), including the well-studied K78A[34] (75% decrease) (Fig. 2g, Extended Data Fig. 7d-f). TRAP L766A, Y772A, and L798A caused over 75% loss of activity stimulation, ~60% for R774A, similar to its partner E168A on TPP1[24], and ~60% for TEN D129A. We next tested whether TPP1 binding defects would affect RAP enhancement by TPP1–POT1. Addition of TPP1-POT1 had little effect on activity but enhanced RAP ~1.4 fold (Extended Data Fig. 7g-i). The TEN–TRAP residue substitutions caused a similar pattern in decreasing stimulation of RAP by TPP1–POT1 to the decreasing stimulation of activity by TPP1 alone (Fig. 2g, Extended Data Fig. 7i). These results

validate the identified interface interactions for TPP1 binding. This first atomic model of the TEN–TRAP interface for TPP1 binding defines the structural requirements for telomerase recruitment and provides a rational basis for drug design to inhibit telomerase action by repressing recruitment.

Features of the catalytic cavity

The TER t/PK forms an oval around the TERT ring that is closed by P1b (Fig. 3a,b). The single-strand region of the t/PK that includes the template wraps along the RBD (5′), RT (template), and CTE (3′), where it passes under the TRAP–TEN (Fig. 3a). In the structure, only the last four bases in the DNA primer d(T_{12}TTAGGG) pair with the template, with the duplex shifted out of the active site as previously reported[8] (Fig. 3b). This observation is consistent with duplexes of four (or five if the active site is occupied) base pairs in *Tetrahymena* telomerase structures at multiple steps of telomere repeat synthesis[10], indicating that a short unstable duplex is a common feature for telomerase[38].

During telomere repeat synthesis, the template movement boundary is determined by an anchor on its 5′ side (template boundary element, TBE)[10,21,39]. In our structure, the perpendicularly positioned P1b-P3 is anchored on TERT RBD by interactions to the single nucleotide junction (C_{186}) and base pairs on either side (Fig. 3c, Extended Data Fig. 4d). This establishes P1b-P3 as the TBE, consistent with mutagenesis results[40]. The template is connected to the TBE by a linker (TBE_L) of eight nucleotides ($U_{38\text{-}43}G_{44}U_{45}$), versus two in *Tetrahymena* telomerase (Fig. 3b, Extended Data Fig. 8a,b). Although $U_{38\text{-}43}$ are loosely tethered as indicated by their weak cryo-EM densities (Extended Data Fig. 8a), $G_{44}U_{45}$ are inserted into a binding pocket on RBD, which appears to be a secondary ‘kedge’ anchor (Fig. 3a, Extended Data Fig. 8c-e). As the template moves, nucleotides in the pocket could pop out and be replaced sequentially by the subsequent residues, up to $U_{41}U_{42}$ when the TBE_L would be fully stretched (Extended Data Fig. 8f). The proposed kedge anchor would help keep the template correctly positioned in the catalytic cavity.

The template–DNA duplex is held in the catalytic cavity by template interactions with motif

3 and fingers on RT and DNA interactions with thumb loop, thumb helix on CTE and T-motif on RBD[8] (Fig. 3d,e, Extended Data Fig. 8g). A bridge loop on RBD, first identified in *Tetrahymena* telomerase and proposed to regulate duplex length[10], bridges the two ends of the duplex with its conserved tip residues (K499, H500; in *Tetrahymena* R413, F414) inserted on the major groove side (Fig. 3d,e). Individual substitutions of these residues to their *Tetrahymena* counterpart had little effect on activity, while substitution with alanine dramatically decreased activity and RAP (Extended Data Fig. 8h). K499, together with Y333 (TFLY), E565 (T) and R622 (fingers), forms a conserved interaction network that regulates stepwise flipping of template bases into the active site (Extended Data Fig. 8i). On the other end of the duplex, the first unpaired DNA nucleotide (dT_{14}) inserts between template nucleotides at the duplex-single-strand junction and interacts with L980 (Fig. 3e). This leucine was proposed to play a major role in strand separation in a very recent publication on human telomerase structure[41]. The following T_{13} flips out and stacks on bridge loop residue H500 (Fig. 3e, Extended Data Fig. 8j). In contrast, in *Tetrahymena* telomerase, all the unpaired DNA nucleotides are stacked continuously under F414 from the bridge loop[10]. This difference may be due to flexibility of the exiting DNA in the absence of telomeric DNA handling protein POT1, versus the constitutively assembled ortholog Teb1 in *Tetrahymena*[21]. Consistent with this, there is no traceable cryo-EM density for DNA nucleotides beyond T_{13}.

On the template 3′-side, the template alignment region enters a narrow, positively charged channel between the TRAP and CTE thumb helix (TRAP–TH channel)[10], and the single-stranded RNA between the template and P2a.1 makes a gooseneck turn below on the CTE (Fig. 3f). The arginines lining the channel could function as a ratchet for template movement during telomere repeat synthesis, as proposed for *Tetrahymena* telomerase[10]. TPP1 binding damps the dynamics of TEN–TRAP, which we propose helps to form the optimal TRAP–TH channel for regulation of telomeric DNA synthesis. Overall, the common features of the human telomerase catalytic cavity to those in *Tetrahymena* suggest a largely conserved mechanism for repeat synthesis and translocation.

TERT–TER interactions scaffold the catalytic core

On the 3' side of the template, the structurally conserved PK forms an irregular helix that wraps around TERT ring from CTE to RBD (Fig. 4a,b). The PK can be divided into three regions: P2a.1 that connects to the single-strand 3′ of the template[32], P2a-P2b that contains a 5 nt asymmetric internal loop (J2a/b), and P2b/P3 that contains conserved base triples from loop-stem interactions[42,43] (Fig. 4a,b, Extended Data Fig. 4a,b). The tertiary structure of P2b/P3 is virtually identical to that determined for this sub-domain in solution[43]. Adjacent to P2b/P3 is a ~90° bend at the 5 nt J2a/b bulge between P2b and P2a[44] and the rest of the P2 stem (P2a.1-P2a-P2b) that passes over the CTE is mostly helical (Fig. 4a,b). The interactions of PK with TERT ring are mainly located on P3 (Extended Data Fig. 4d), which fits into the positively charged cleft between CTE and RBD (Fig. 4a, Extended Data Fig. 9a). Surprisingly, except for a flipped out G_{73} between P2a.1-P2a and C_{116} at the P2b-P3 junction, the entire P2 only contacts TERT at its 5' end, where P2a.1 abuts a positively charged surface of TEN on its major groove side (Fig. 4b, Extended Data Fig. 9a). While P2b/P3 is fixed on TERT, the rest of the PK exhibits conformational dynamics, as revealed by modeling of different class averages (Extended Data Fig. 9b-e).

Besides the interactions from P3, the TERT ring is further stabilized by CR4/5 binding from the opposite side. In CR4/5, P6 is stacked on P5.1—a predicted 3 bp helix[36,45] formed by interactions in the large internal loop between P6, P5, and P6.1—and P6.1 hairpin is perpendicular to P6 (Fig. 4c, Extended Data Fig. 4a,c,e). The highly conserved P6.1 hairpin bridges the RBD and CTE, while P6 binds RBD as observed in teleost fish[46] (Fig. 4c). Together, CR4/5 and PK form a framework that inhibits large-scale conformational change in the TERT ring (Fig. 4b).

A single bulge nucleotide (U_{177}) below the three U-A-U triples[42,43] in P2b/P3 is within ~7Å of U_{307} on P6.1 hairpin loop in CR4/5 (Fig. 4d, Extended Data Fig. 4d,e). Our model reveals these two nucleotides bind in separate pockets on opposite sides of CTE, separated by loop $L_{\alpha 32\text{-}\alpha 33}$ (aa 1019-1028). U_{177} base interacts with four $L_{\alpha 32\text{-}\alpha 33}$ residues, including L1019, while

U_{307} hydrogen bonds with Q1023 (Fig. 4d, Extended Data Fig. 4d,e). Disease mutations L1019F (pulmonary fibrosis), V1025F and V1090M[13] (aplastic anemia), and N1028H (DKC) would disrupt interactions that stabilize P2b/P3 and/or P6.1 binding to CTE in this region. Docking of telomerase-specific inhibitor BIBR1532 onto its binding site on CTE, based on homology to CTE of *Tribolium* TERT-like protein[11], reveals that its benzoic ring would occlude U_{177} binding and its naphthalene group repositions $L_{\alpha 32\text{-}\alpha 33}$, which could also affect P6.1 interaction (Fig. 4d). Thus, as a non-nucleosidic telomerase inhibitor[12], BIBR1532 disrupts critical TERT–TER interactions, making it the first known example of a drug targeting a non-template region of TER[47].

Insights into catalytic core disease mutations

Over 185 and 75 mutations in TERT and TER, respectively, lead to short telomeres and manifest as diseases of telomerase insufficiency[13]. In TER, the vast majority of these are in the PK and CR4/5, and there are only a few in the H/ACA RNA[13]. We mapped known disease-associated mutations of TER and TERT (that would not obviously disrupt TERT hydrophobic core) onto the structure (Fig. 5, center). Almost all TER mutations in the catalytic core contact or are adjacent to nucleotides that contact TERT. Notably, there are many mutations in PK P3 and P1b (Fig. 5, Extended Data Fig. 4d,e). A few others would affect critical folds such as the conserved 90° bend in the J2a/b loop[44] by disruption of stem base pairs (Extended Data Fig. 4a). The 3.3Å model of the catalytic core reveals specific TERT–TER contacts that would be affected by individual mutations (Fig. 5, boxed examples). For pulmonary fibrosis, examples include mutations in TERT RT fingers (R622C) and TRAP (R756L) motifs that would disrupt interactions with the template. Fingers R622 is part of the conserved network of residues that regulates sequential flipping of the template nucleotides opposite the active site (Fig. 3e)[8,10]. R756 is at the top of the TRAP–TH channel where it stacks with template (A_{55}) and helps regulate the one-way movement of the template during nucleotide addition (Fig. 3f). CTE mutation R1086C would disrupt interactions with the backbone of P2b C_{116}, the last residue of P2b/P3 pseudoknot to interact with TERT (Extended Data Fig. 4d). Dyskeratosis congenita TER mutations include G73U; G_{73} is the single residue at the P2a.1-J2a/b junction that specifically

interacts with CTE (Fig. 4b). Mutations throughout the pseudoknot P3 that have direct contacts with TERT or stabilize the extended P3 stem (Extended Data Fig. 4d), are associated with aplastic anemia and other diseases[13]. Aplastic anemia TER mutation G305U would disrupt the top of P6.1 and interaction with CTE Q1023, and TH R979Y would affect template handling in the TRAP–TH channel (Fig. 5). Acute myeloid leukemia G309U (P6.1) and myelodysplastic syndrome R535H (RBD) provide additional examples of mutations that would disrupt P6.1–TERT interactions, with CTE Q1023 and P6.1 A_{302}, respectively. Dyskeratosis congenita R381P (RBD) would disrupt arginine interactions with 3 base pairs flanking the bulged U_{291} in CR4/5 helix P6. Lastly, K570N (RBD T motif) is associated with Hoyeraal-Hreidarsson syndrome (Fig. 5) and pulmonary fibrosis; K570 interacts with the DNA backbone in the template–DNA duplex (Fig. 3e). Analysis of these interactions validates the importance for telomerase activity of the TERT–TER interactions defined in our model and provides a structural basis for drug targeting.

Summary

This first structure of human telomerase in complex with shelterin protein TPP1 illustrates the detailed interface essential for recruitment and activation. Our comparison of common and divergent features of the catalytic cores of *Tetrahymena*[10] and human telomerase at 3.3Å resolution has unveiled details of template–DNA handling, template boundary definition, and duplex length during telomere repeat addition. TPP1 binding stabilizes the TRAP–TEN interface and TRAP–TH channel, and its association with POT1 positions it to bind the newly synthesized telomeric DNA. Analysis of disease mutations as well as the binding site for the telomerase-specific inhibitor BIBR1532[11,12] revealed the critical importance of TERT–TER interactions for telomerase activity and as potential drug targets. Overall, these findings provide a basis for structure-guided telomerase-targeted drug discovery and a deeper understanding of disease mutations leading to telomere biology disorders.

Main References

1 Blackburn, E. H. & Collins, K. Telomerase: an RNP enzyme synthesizes DNA. *Cold Spring Harb Perspect Biol* **3** (2011).

2 Chakravarti, D., LaBella, K. A. & DePinho, R. A. Telomeres: history, health, and hallmarks of aging. *Cell* **184**, 306-322 (2021).

3 Trybek, T., Kowalik, A., Gozdz, S. & Kowalska, A. Telomeres and telomerase in oncogenesis. *Oncol Lett* **20**, 1015-1027 (2020).

4 Roake, C. M. & Artandi, S. E. Regulation of human telomerase in homeostasis and disease. *Nat Rev Mol Cell Biol* **21**, 384-397 (2020).

5 Shay, J. W. Role of Telomeres and Telomerase in Aging and Cancer. *Cancer Discov* **6**, 584-593 (2016).

6 Aramburu, T., Plucinsky, S. & Skordalakes, E. POT1-TPP1 telomere length regulation and disease. *Comput Struct Biotechnol J* **18**, 1939-1946 (2020).

7 de Lange, T. Shelterin-Mediated Telomere Protection. *Annu Rev Genet* **52**, 223-247 (2018).

8 Ghanim, G. E. *et al.* Structure of human telomerase holoenzyme with bound telomeric DNA. *Nature* **593**, 449-453 (2021).

9 Nguyen, T. H. D. *et al.* Cryo-EM structure of substrate-bound human telomerase holoenzyme. *Nature* **557**, 190-195 (2018).

10 He, Y. *et al.* Structures of telomerase at several steps of telomere repeat synthesis. *Nature* **593**, 454-459 (2021).

11 Bryan, C. *et al.* Structural Basis of Telomerase Inhibition by the Highly Specific BIBR1532. *Structure* **23**, 1934-1942 (2015).

12 Pascolo, E. *et al.* Mechanism of human telomerase inhibition by BIBR1532, a synthetic, non-nucleosidic drug candidate. *J Biol Chem* **277**, 15566-15572 (2002).

13 Podlevsky, J. D., Bley, C. J., Omana, R. V., Qi, X. & Chen, J. J. The telomerase database. *Nucleic Acids Res* **36**, D339-343 (2008).

14 Holohan, B., Wright, W. E. & Shay, J. W. Cell biology of disease: Telomeropathies: an emerging spectrum disorder. *J Cell Biol* **205**, 289-299 (2014).

15 Wu, R. A., Upton, H. E., Vogan, J. M. & Collins, K. Telomerase Mechanism of Telomere Synthesis. *Annu Rev Biochem* **86**, 439-460 (2017).

16 Schmidt, J. C. & Cech, T. R. Human telomerase: biogenesis, trafficking, recruitment, and activation. *Genes Dev* **29**, 1095-1105 (2015).

17 Grill, S. & Nandakumar, J. Molecular mechanisms of telomere biology disorders. *J Biol Chem* **296**, 100064 (2021).

18 Schratz, K. E. *et al.* Cancer spectrum and outcomes in the Mendelian short telomere syndromes. *Blood* **135**, 1946-1956 (2020).

19 Reilly, C. R. *et al.* The clinical and functional effects of TERT variants in myelodysplastic syndrome. *Blood* **138**, 898-911 (2021).

20 Jiang, J. *et al.* Structure of Telomerase with Telomeric DNA. *Cell* **173**, 1179-1190 e1113 (2018).

21 Jiang, J. *et al.* Structure of Tetrahymena telomerase reveals previously unknown subunits, functions, and interactions. *Science* **350**, aab4070 (2015).

22 Lim, C. J. & Cech, T. R. Shaping human telomeres: from shelterin and CST complexes to telomeric chromatin organization. *Nat Rev Mol Cell Biol* **22**, 283-298 (2021).

23 Lei, M., Podell, E. R. & Cech, T. R. Structure of human POT1 bound to telomeric single-stranded DNA provides a model for chromosome end-protection. *Nat Struct Mol Biol* **11**, 1223-1229 (2004).

24 Nandakumar, J. *et al.* The TEL patch of telomere protein TPP1 mediates telomerase recruitment and processivity. *Nature* **492**, 285-289 (2012).

25 Zhong, F. L. *et al.* TPP1 OB-fold domain controls telomere maintenance by recruiting telomerase to chromosome ends. *Cell* **150**, 481-494 (2012).

26 Sexton, A. N., Youmans, D. T. & Collins, K. Specificity requirements for human telomere protein interaction with telomerase holoenzyme. *J Biol Chem* **287**, 34455-34464 (2012).

27 Grill, S., Tesmer, V. M. & Nandakumar, J. The N Terminus of the OB Domain of Telomere Protein TPP1 Is Critical for Telomerase Action. *Cell Rep* **22**, 1132-1140 (2018).
28 Chen, C. *et al.* Structural insights into POT1-TPP1 interaction and POT1 C-terminal mutations in human cancer. *Nat Commun* **8**, 14929 (2017).
29 Rice, C. *et al.* Structural and functional analysis of the human POT1-TPP1 telomeric complex. *Nat Commun* **8**, 14928 (2017).
30 Schmidt, J. C., Zaug, A. J. & Cech, T. R. Live Cell Imaging Reveals the Dynamics of Telomerase Recruitment to Telomeres. *Cell* **166**, 1188-1197 e1189 (2016).
31 Mitchell, J. R., Cheng, J. & Collins, K. A box H/ACA small nucleolar RNA-like domain at the human telomerase RNA 3' end. *Mol Cell Biol* **19**, 567-576 (1999).
32 Zhang, Q., Kim, N. K. & Feigon, J. Architecture of human telomerase RNA. *Proc Natl Acad Sci U S A* **108**, 20325-20332 (2011).
33 Wang, F. *et al.* The POT1-TPP1 telomere complex is a telomerase processivity factor. *Nature* **445**, 506-510 (2007).
34 Schmidt, J. C., Dalby, A. B. & Cech, T. R. Identification of human TERT elements necessary for telomerase recruitment to telomeres. *Elife* **3** (2014).
35 Tesmer, V. M., Smith, E. M., Danciu, O., Padmanaban, S. & Nandakumar, J. Combining conservation and species-specific differences to determine how human telomerase binds telomeres. *Proc Natl Acad Sci U S A* (2019).
36 Wang, Y., Gallagher-Jones, M., Susac, L., Song, H. & Feigon, J. A structurally conserved human and Tetrahymena telomerase catalytic core. *Proc Natl Acad Sci U S A* **117**, 31078-31087 (2020).
37 Hong, K. *et al.* Tetrahymena telomerase holoenzyme assembly, activation, and inhibition by domains of the p50 central hub. *Mol Cell Biol* **33**, 3962-3971 (2013).
38 Forstemann, K. & Lingner, J. Telomerase limits the extent of base pairing between template RNA and telomeric DNA. *EMBO Rep* **6**, 361-366 (2005).
39 Jansson, L. I. *et al.* Structural basis of template-boundary definition in Tetrahymena telomerase. *Nat Struct Mol Biol* **22**, 883-888 (2015).
40 Chen, J. L. & Greider, C. W. Template boundary definition in mammalian telomerase. *Genes Dev* **17**, 2747-2752 (2003).
41 Wan, F. *et al.* Zipper head mechanism of telomere synthesis by human telomerase. *Cell Res* **31**, 1275-1290 (2021).
42 Theimer, C. A., Blois, C. A. & Feigon, J. Structure of the human telomerase RNA pseudoknot reveals conserved tertiary interactions essential for function. *Mol Cell* **17**, 671-682 (2005).
43 Kim, N. K. *et al.* Solution structure and dynamics of the wild-type pseudoknot of human telomerase RNA. *J Mol Biol* **384**, 1249-1261 (2008).
44 Zhang, Q., Kim, N. K., Peterson, R. D., Wang, Z. & Feigon, J. Structurally conserved five nucleotide bulge determines the overall topology of the core domain of human telomerase RNA. *Proc Natl Acad Sci U S A* **107**, 18761-18768 (2010).
45 Palka, C., Forino, N. M., Hentschel, J., Das, R. & Stone, M. D. Folding heterogeneity in the essential human telomerase RNA three-way junction. *RNA* **26**, 1787-1800 (2020).
46 Huang, J. *et al.* Structural basis for protein-RNA recognition in telomerase. *Nat Struct Mol Biol* **21**, 507-512 (2014).
47 Guterres, A. N. & Villanueva, J. Targeting telomerase for cancer therapy. *Oncogene* **39**, 5811-5824 (2020).

Materials and Methods

Telomerase expression and purification Human telomerase was reconstituted *in vivo* and purified largely as previously reported[9], except for the addition of an initial IgG affinity purification step. Briefly, human TERT and TER genes from plasmid pBABEpuroUThTERT+U3-hTR-500[48] (AddGene) were individually cloned into pcDNA3.1 vectors, and pcDNA3.1-ZZ-TEV-SS-TERT and pcDNA3.1-U3-TER-500ex-HDV were constructed as described[9]. For the TERT plasmid, a tobacco etch virus (TEV) protease cleavage site was inserted between the tandem Protein A (ZZ) and TwinStrep (SS) tag (IBA Lifesciences) cassettes for telomerase purification. For the TER plasmid, the U3 snoRNA promoter[49] was inserted before TER and a 500-nt extended sequence[50] was inserted between TER and hepatitis delta virus ribozyme (HDV)[51]. We used adherent HEK 293T cells for telomerase reconstitution. The cells were cultured on 150 mm plates with DMEM media (Gibco) supplemented with 10% FBS (Atalanta), 1% Pen-Strep, and 1% GlutaMAX. The cells were transfected with an optimal ratio of 1:4 of TERT and TER plasmids using calcium phosphate reagents[52]. After 48 hours of transfection, the cells were harvested by centrifugation (1000x g, 5 min) and resuspended in pre-chilled hypotonic lysis buffer (HLB) (20 mM HEPES·NaOH pH 8.0, 10% glycerol, 2 mM EDTA, 0.2 mM EGTA, and 1 mM TCEP) supplemented with 0.1% NP-40, 0.2 mM PMSF, 10 μM MG-132 (Sigma), and 0.2% protease inhibitor cocktail (Sigma). Cells were incubated on ice for 10 min before being flash frozen and stored at -80°C.

For telomerase purification, frozen cells from 120 plates were thawed and subjected to two additional freeze-thaw cycles. The cell lysate was adjusted to 300 mM NaCl concentration and incubated on ice for 30 min. An equivalent volume of HLB buffer supplemented with 0.1% Igepal CA-630 was added to the cell extract to dilute the NaCl concentration to 150 mM. The cell lysate was cleared by ultracentrifugation (125,000x g) for 1 hour at 4°C. The prepared cell lysate was incubated with IgG resin (Sigma) for 5 hours at 4°C with end-over-end rotation. The resin was washed three times with wash buffer (20 mM HEPES·NaOH pH 8.0, 150 mM NaCl, 10% glycerol, 2 mM EDTA, 0.2 mM EGTA, 1 mM TCEP, and 0.1% Igepal CA-630) before elution by

TEV protease cleavage at 4°C for 1 hour. The eluate was subsequently incubated with streptavidin agarose resin (Sigma) prebound to a 5′-biotinylated oligonucleotide[53] at room temperature for 2.5 hours. The resin was washed with wash buffer and eluted with 50 μM competitor oligonucleotide[53] in 500 μl wash buffer three times. The total elution was further incubated with pre-blocked MagStrep XT3 resin (IBA LifeSciences) overnight at 4°C along with 5 μM DNA primer, T_{12}TTAGGG. The resin was washed with wash buffer and eluted with 35 μl biotin elution buffer (20 mM HEPES·NaOH pH 8.0, 150 mM NaCl, 2 mM $MgCl_2$, 20 mM biotin, 1 mM TCEP, and 0.05% Igepal CA-630) to get the final product.

TPP1 expression and purification TPP1 OB (residues 88-249) and TPP1 OB-PBD (residues 88-334, Addgene) were cloned into a modified pETduet vector with an N-terminal 6xHis-MBP tag followed by a TEV protease cleavage site and a pET-SUMO vector individually. The proteins were expressed in *Escherichia coli* BL21 (DE3) cells as described[33]. LB media with 100 μg/ml Ampicillin (for TPP1 OB) or 50 μg/ml Kanamycin (for TPP1 OB-PBD) were used for bacterial growth at 37°C to an OD_{600} of 0.6. Protein expression was induced by 0.5 mM IPTG for 20 hours at 18°C. Cells were harvested, suspended in buffer A (20 mM HEPES·NaOH pH 8.0, 1 M NaCl, 15 mM Imidazole, 5% glycerol, and 1 mM TCEP), sonicated and centrifuged at 34,000x g for 45 min. The supernatant was loaded onto a Ni-Sepharose affinity column (HisTrap HP; GE Healthcare). The column was washed with 95% buffer A and 5% buffer B (20 mM HEPES·NaOH pH 8.0, 0.5 M NaCl, 1 M Imidazole, 5% glycerol, and 1 mM TCEP), and then the protein was eluted with 70% buffer A and 30% buffer B. The eluate was incubated with TEV protease (for TPP1 OB) or SUMO protease (for TPP1 OB-PBD) for 3-4 hours at room temperature while dialyzing against buffer containing 20 mM Tris·HCl pH 7.5, 250 mM NaCl, and 5 mM β-mercaptoethanol. TPP1 was collected from the flow through after loading the cleavage reaction onto a Ni-Sepharose affinity column. Further purification was conducted by size-exclusion chromatography (SEC) (HiLoad 26/600 Superdex 75; GE Healthcare) in SEC buffer (20 mM HEPES·NaOH pH 8.0, 150 mM NaCl, 5% glycerol, and 1 mM TCEP). TPP1 OB protein peak fractions were pooled and concentrated to 300 μM using 10 KDa cut-off Amicon

filters (Millipore Sigma), then aliquoted and stored at -80°C. To prepare the TPP1 bound telomerase, a final concentration of 500 nM purified TPP1 OB was added to the purified telomerase and incubated on ice for 1 hour just prior to grid preparation.

TPP1-POT1 complex purification POT1 was expressed using the Bac-to-Bac system (Thermo Fisher Scientific) in *Sf9* cells. Briefly, cDNAs encoding POT1 was chemically synthesized by IDT (Integrated DNA Technologies, Inc.) and cloned into pFastBac1 vector (Thermo Fisher Scientific) with an N-terminal 6xHis-MBP tag followed by a TEV protease cleavage site. The expression vectors were used to make baculoviruses based on the established protocol for Bac-to-Bac system (Thermo Fisher Scientific). *Sf9* cells (2.0×10^6/ml) were transfected with viruses using a multiplicity of infection (MOI) of 3 at 27°C in SF-900^{TM} II SFM media (Thermo Fisher Scientific). The cells were harvested 48 h after infection, and proteins were purified as described for TPP1. Fractions of POT1 collected from SEC (HiLoad 26/600 Superdex 200; GE Healthcare) were mixed with TPP1 OB-PBD at 1:1 ratio and incubated at 4°C for 1 hour before loaded to another SEC. TPP1-POT1 fractions were collected and concentrated to ~100 μM using 30 KDa cut-off Amicon filters (Millipore Sigma), then aliquoted and stored at -80°C.

Cryo-EM sample preparation and data collection Telomerase samples were applied to glow-discharged lacey gold grids coated with a supporting ultrathin carbon film (EMS). The grids were blotted with Grade 595 filter paper (Ted Pella) and flash-frozen in liquid ethane using an FEI Vitrobot Mark IV. Cryo-EM grids prepared and frozen with varying parameters (including the time and gas for glow-discharging, the volume of applied sample, temperature and humidity of the Vitrobot sample chamber, waiting time before blotting, blotting time and force) were screened in an FEI Tecnai TF20 transmission electron microscope for optimal ice thickness, particle concentration and particle distribution on grids. The best grids were obtained with 30 s glow-discharging in mixed H_2 and O_2, 5 μL sample applied on each grid, and Vitrobot set at 10°C, 100% humidity, waiting time 4 min, blotting force 4, and blotting time 10 s.

Cryo-EM grids were loaded into a ThermoFisher Titan Krios electron microscope operated at 300 kV for automated data collection using SerialEM[54]. Movies of dose-fractionated

443 frames were acquired with a Gatan K3 direct electron detector in super-resolution mode at a
444 pixel size of 0.55 Å on the sample level. A Gatan Imaging Filter (GIF) was installed between the
445 electron microscope and the K3 camera with the slit width setting to 20 eV. The microscope was
446 carefully aligned prior to each imaging session and the parallel beam was optimized using
447 coma-free alignment in SerialEM[54]. The dose rate on the sample was set to ~ 55 electrons/Å^2 in
448 total, which was fractionated into 50 frames with 0.06 s exposure time for each frame. Finally,
449 31,728 movies were collected in three separate imaging sessions with three batches of cryo-EM
450 grids (Extended Data Fig. 1).
451 ***Cryo-EM data processing*** The cryo-EM data processing workflow is outlined in Extended Data
452 Fig. 1. All steps described below were performed with RELION 3.1[55] unless otherwise indicated.
453 Dose-fractionated frames of each movie were 2x binned (pixel size of 1.1 Å), aligned for the
454 correction of beam-induced drift, and dose weighted using RELION's implementation of UCSF
455 MotionCor2[56]. Contrast transfer function (CTF) parameters, including defocus and astigmatism,
456 of each dose-weighted micrograph were determined by CTFFIND4[57] within RELION.
457 Three datasets, one for each data collection session, were initially processed separately
458 in three batches (Extended Data Fig. 1a). For dataset1, 666,560 particles were picked from
459 2,000 representative micrographs using template-free auto-picking in RELION. There particles
460 were extracted in boxes of 384^2 square pixels and 3x binned to 128^2 square pixels (pixel size of
461 3.3 Å) for 2D classification. 203,042 particles from the best classes were selected to train a
462 particle detection model in Topaz[58] for subsequent neural-network based particle picking. From
463 the 16,244 micrographs of dataset1 a total of 8,500,796 particles were picked, 3x binned and
464 extracted in boxes of 128^2 square pixels (pixel size of 3.3 Å). Two rounds of 2D classification
465 were performed to remove "bad" particles in classes with fuzzy or uninterpretable densities.
466 3,006,138 particles in classes with clear features for both the catalytic core and H/ACA RNP
467 were selected. Refinement of the selected particles using a previously published cryo-EM map[9]
468 (EMD-7521) as an initial model generated a 3D reconstruction with only low-resolution features.
469 To improve the resolution, each particle was re-extracted into two sub-particles with shifted

origins (RELION option: --recenter_x/y/z), one centered on the catalytic core and the other centered on the H/ACA RNP. Sub-particles centered on the catalytic core were extracted in boxes of 128^2 square pixels (pixel size of 2.2 Å) and refined using a soft mask encasing the catalytic core (mask1). The resulting orientation parameters for each sub-particle were used as inputs for the subsequent masked 3D classification step with local angular search (RELION options: --sigma_ang 30 --healpix_order 2). In parallel, sub-particles centered on the H/ACA RNP were extracted in boxes of 200^2 square pixels (pixel size of 2.2 Å), refined and 3D classified with a soft mask covering the H/ACA RNP (mask2). An additional step of 2D classification was performed before 3D refinement to remove sub-particles that were not centered properly on the H/ACA RNP. Lastly, 1,781,404 sub-particles centered on the catalytic core and 1,055,677 sub-particles centered on the H/ACA RNP were selected from dataset1.

Dataset2 and dataset3 were processed in a similar way as described above for dataset1 (Extended Data Fig. 1a). For dataset2, 4,413,286 particles were picked from 8,361 micrographs. After screening, 429,103 sub-particles centered on the catalytic core and 439,516 sub-particles centered on the H/ACA RNP were selected. For dataset3, 2,641,248 particles were picked from 7,123 micrographs. 403,764 sub-particles centered on the catalytic core and 504,954 sub-particles centered on the H/ACA RNP were selected after screening. The two types of sub-particles from the three datasets were combined and processed respectively with the following steps.

For the H/ACA RNP, the combined 2,000,147 sub-particles (pixel size of 2.2 Å) were refined to 4.4 Å resolution using mask2 (Extended Data Fig. 1c). Then, two rounds of 3D classification were performed with local angular search in 30° (RELION options: --sigma_ang 30 --healpix_order 2) and 12° (RELION options: --sigma_ang 12 --healpix_order 3), respectively. 432,108 sub-particles from the best class were extracted in boxes of 320^2 (pixel size of 1.1 Å) and refined to 3.3 Å resolution. After another round of 3D classification with a finer angular sampling interval (RELION options: --sigma_ang 8 --healpix_order 4), 256,859 sub-particles were selected for 3D refinement, following by CTF refinement to correct CTF parameters,

anisotropic magnification and higher-order aberrations. Beam-induced particle motions were corrected using Bayesian polishing module in RELION. The resulting “shiny” particles were refined with mask2, resulting in a final 3.2 Å resolution reconstruction of the H/ACA RNP module (Extended Data Fig. 2a, b, d).

For the catalytic core, the combined 2,614,217 sub-particles (pixel size of 2.2 Å) were refined to 4.4 Å resolution using mask1 (Extended Data Fig. 1d), and then classified into six classes (RELION options: --sigma_ang 20 --healpix_order 3). 1,386,006 sub-particles from the two best classes were combined, extracted in boxes of 256^2 (pixel size of 1.1 Å), and refined to 3.4 Å resolution. Notably, the cryo-EM densities of the TEN domain of TERT and P2a.1-P2a of TER were weaker than the rest in the resulting map, suggesting that they are positionally flexible and/or adopt more than one conformation. The sub-particles were therefore subjected to another round of 3D classification with a finer angular sampling (RELION options: --sigma_ang 6 --healpix_order 4) and a tighter soft mask (mask3) to exclude the flexible regions described above. 291,504 sub-particles from the best class were selected for 3D refinement, CTF refinement and Bayesian polishing. The resulting “shiny” sub-particles were refined to 3.3 Å resolution with mask1 for the entire catalytic core and to 3.2 Å resolution with mask3 for the rigid region that excludes TEN and P2a.1-P2a (Extended Data Fig. 2a, c, e). Several alignment-free 3D classifications using different masks (Extended Data Fig. 3) were subsequently performed to investigate the compositional and conformational heterogeneities within the catalytic core, as described below.

To separate sub-particles bound with H2A-H2B heterodimer, a soft mask covering the junction region of P2b, P6.1 and P6 was used in the 3D classification (Extended Data Fig. 3a). The input 291,504 sub-particles were classified into 10 classes with an optimized regularisation parameter (RELION option: --tau2_fudge 8). A subset of 65,345 sub-particles (21.9% of the inputs) in one class with clear features for the H2A-H2B were selected and refined to 3.7 Å resolution using mask1 (Extended Data Fig. 3a).

To separate sub-particles bound with TPP1, the inputs were classified into 4 classes with a spherical soft mask covering the space above the TEN-TRAP (Extended Data Fig. 3a). A subset of 118,845 sub-particles in one class with the best density for TPP1 were selected and refined to 3.5 Å resolution (Extended Data Fig. 3a, c, d). Meanwhile, 83,992 sub-particles from another class without TPP1 were refined to 3.7 Å resolution. These two subsets of catalytic core sub-particles were further classified into six classes, respectively, with a soft mask encasing the P2a.1-P2a of TER (Extended Data Fig. 3a). The resulting classes with interpretable features (i.e., major and minor grooves of the RNA duplex) were refined individually.

Resolutions of the cryo-EM maps were estimated on the basis of the "gold-standard" Fourier Shell Correlation (FSC) = 0.143 criterion[59]. The cryo-EM maps were corrected for the modulation transfer function of the detector, sharpened with a negative B-factor and low-pass filtered to the stated resolution using the *relion_postprocess* program in RELION. Local resolution evaluations were determined by RELION with two independently refined half-maps. Data collection and processing statistics are given in Extended Data Table 1.

Model building and refinement The atomic models of human telomerase catalytic core were built and refined manually in COOT[60]. The 3.3 Å resolution cryo-EM map of catalytic core (Extended Data Fig. 1d) was used for the modeling of TERT RBD-RT-CTE ring and associated TER CR4/5 and t/PK except for the P2a.1 and P2a. The 3.5 Å resolution map of catalytic core bound with TPP1 was used for the modeling of TERT TEN–TRAP, TER P2a and P2a.1, as well as TPP1. The 3.7 Å resolution map of catalytic core bound with H2A-H2B was used for the modeling of H2A and H2B.

Initially, our refined model of human telomerase catalytic core[36] based on a reported 8 Å resolution cryo-EM map[9] was fitted into the current catalytic core maps with UCSF Chimera[61] as a beginning for model building. The high-resolution features of the current map provided more accurate main chain and most side chain conformations (Extended Data Fig. 2g-j), which aided the side chain adjustment even main chain re-tracing when necessary to get the close fit between the density and the model. Visible densities of amino acid residues with bulky side

chains, such as Phe, Tyr and Trp were used as guidance for sequence assignment. No density was observed for the linker between TEN and RBD (residues 179-321), RBD residues 417-443, and RT residues 641-650, so these residues were not modeled. The crystal structure of TPP1-OB (PDB: 2I46)[33] was fitted into the telomerase–TPP1 sub-class maps and manually refined in a similar way (Extended Data Fig. 3f). The H2A-H2B heterodimer (Extended Data Fig. 3b) was adapted from the structure of human telomerase holoenzyme (PDB: 7BG9)[8] published during the preparation of this manuscript. Comparison of our model to that of Ghanim et al (2021) revealed some differences in residue register (about 16% overall for visible regions of TERT), especially within the TEN (37%). Our telomerase–TPP1 structure exhibits less positional dynamics and therefore higher resolution for TEN–TRAP, while the higher resolution of the catalytic core in the combined maps provided better density for backbone and sidechain positioning for the TERT ring and associated TER.

TER regions contacting TERT, especially the t/PK domain and P6.1 stem, were de novo built due to the well-defined nucleotide densities (Extended Data Fig. 2i). Other parts of TER were adjusted from our previous model[36] for their base conformations and backbones to fit into the density map. The different conformations of the most flexible region of TER (P2a.1-P2a) were achieved from different classes of local refined maps in a similar way (Extended Data Fig. 3a). The substrate DNA was traced from the 3′ end inside the catalytic cavity with seven nucleotides modeled including the G_{18}-A_{15} which form a four base pair duplex with the template. Nucleotides T_1-T_{11} were invisible in the cryo-EM map.

For the modeling of H/ACA RNP, the previously published model (PDB: 7BGB)[8] was used as the starting point. The model was rigid-body fitted into our 3.2 Å resolution cryo-EM map of H/ACA RNP and adjusted manually in COOT.

Catalytic core and H/ACA RNP models were refined individually using Phenix[62] in real space with secondary structure, Ramachandran, and rotamer restraints. All structures were validated using the Molprobity scores and statistics of the Ramachandran plots. Refinement statistics of the models are summarized in Extended Data Table 1. Model vs map FSC

validation is shown in Extended Data Fig. 2-3. All figures presenting the model were prepared using UCSF Chimera[61], ChimeraX[63], and PyMOL[64].

In Vitro Reconstitution of Telomerase and Direct Telomerase Activity Assays Human TER for telomerase activity assays was prepared as described for *Tetrahymena* TER[10], with minor changes. Briefly, TER was in vitro transcribed with homemade T7 RNA polymerase (P226L mutant)[65] using 1 μM linearized pUC19-T7-TER template in a reaction containing 40 mM Tris·HCl pH 8.0, 5 mM of each dNTP, 40 mM $MgCl_2$, 1 mM spermidine, 2.5 mM DTT, and 0.01% Triton X-100. The reaction was performed at 37°C for 4 hours. Product was purified with a 10% denaturing polyacrylamide gel followed by electroelution. Human telomerase catalytic core (TERT and TER) was reconstituted in RRL as described[44,66] with minor changes. Wild type (WT) and mutant human TERTs were expressed in RRL using the TNT quick coupled transcription/translation system (Promega) for 2 hours before incubation with 1 μM TER with and without 10 μM TPP1 (or 0.25 μM TPP1-POT1 as noted) for another 30 min. The concentration of TPP1 and TPP1-POT1 used in assays were optimized under linear conditions. Assays were performed in a 20 μl reaction volume containing 25 mM Tris·HCl pH 8.3, 2 mM $MgCl_2$, 1 mM DTT, 500 μM dTTP, 500 μM dATP, 12.5 μM dGTP, and 3-5 μCi α-^{32}P-dGTP (Perkin-Elmer), 500 nM DNA primer $d(TTAGGG)_3$ and 10 μl of telomerase reconstituted from RRL. After 1 hour incubation at 37°C, reactions were stopped by adding 80 μl quench buffer (10 mM Tris·HCl, pH 8.0, and 10 mM EDTA) supplied with a 15 nt ^{32}P-end-labelled primer as a recovery control (RC). Products were phenol-chloroform extracted, ethanol precipitated, and resolved on a 10% denaturing polyacrylamide gel. The gel was vacuum dried and exposed to a phosphor imaging screen for 20 hours. The final image was obtained by scanning the screen on a ImageFX system (Bio-Rad) and then quantified with QuantityOne (Bio-rad).Telomerase activity and repeat addition processivity (RAP) were determined as previously described[10]. The integrated intensity of each lane was used for calculation of telomerase activity and intensities of bands representing the extension of one telomere repeat processed using the “fraction left behind” (FLB) method[67,68] for calculation of telomerase RAP (Supplementary Fig. 1). WT TERT

without TPP1 was set as 1 for both activity and RAP, while WT with TPP1 along with all other mutants were compared to it for relative activity and RAP. Activity stimulation was calculated by Relative activity with TPP1 / Relative activity without TPP1. Activity stimulation loss was calculated as (Activity stimulation of WT TERT minus Activity stimulation of mutant TERT) / (Activity stimulation of WT TERT minus 1).

Methods References

8 Ghanim, G. E. *et al.* Structure of human telomerase holoenzyme with bound telomeric DNA. *Nature* **593**, 449-453 (2021).

9 Nguyen, T. H. D. *et al.* Cryo-EM structure of substrate-bound human telomerase holoenzyme. *Nature* **557**, 190-195 (2018).

10 He, Y. *et al.* Structures of telomerase at several steps of telomere repeat synthesis. *Nature* **593**, 454-459 (2021).

11 Bryan, C. *et al.* Structural Basis of Telomerase Inhibition by the Highly Specific BIBR1532. *Structure* **23**, 1934-1942 (2015).

13 Podlevsky, J. D., Bley, C. J., Omana, R. V., Qi, X. & Chen, J. J. The telomerase database. *Nucleic Acids Res* **36**, D339-343 (2008).

33 Wang, F. *et al.* The POT1-TPP1 telomere complex is a telomerase processivity factor. *Nature* **445**, 506-510 (2007).

36 Wang, Y., Gallagher-Jones, M., Susac, L., Song, H. & Feigon, J. A structurally conserved human and Tetrahymena telomerase catalytic core. *Proc Natl Acad Sci U S A* **117**, 31078-31087 (2020).

44 Zhang, Q., Kim, N. K., Peterson, R. D., Wang, Z. & Feigon, J. Structurally conserved five nucleotide bulge determines the overall topology of the core domain of human telomerase RNA. *Proc Natl Acad Sci U S A* **107**, 18761-18768 (2010).

48 Wong, J. M. & Collins, K. Telomerase RNA level limits telomere maintenance in X-linked dyskeratosis congenita. *Genes Dev* **20**, 2848-2858 (2006).

49 Gao, L., Frey, M. R. & Matera, A. G. Human genes encoding U3 snRNA associate with coiled bodies in interphase cells and are clustered on chromosome 17p11.2 in a complex inverted repeat structure. *Nucleic Acids Res* **25**, 4740-4747 (1997).

50 Fu, D. & Collins, K. Distinct biogenesis pathways for human telomerase RNA and H/ACA small nucleolar RNAs. *Mol Cell* **11**, 1361-1372 (2003).

51 Ferre-D'Amare, A. R., Zhou, K. & Doudna, J. A. Crystal structure of a hepatitis delta virus ribozyme. *Nature* **395**, 567-574 (1998).

52 Chen, Y. Calcium Phosphate Transfection of Eukaryotic Cells. *Bio-Protocol* **2** (2012).

53 Kurth, I., Cristofari, G. & Lingner, J. An affinity oligonucleotide displacement strategy to purify ribonucleoprotein complexes applied to human telomerase. *Methods Mol Biol* **488**, 9-22 (2008).

54 Mastronarde, D. N. Automated electron microscope tomography using robust prediction of specimen movements. *J Struct Biol* **152**, 36-51 (2005).

55 Zivanov, J. *et al.* New tools for automated high-resolution cryo-EM structure determination in RELION-3. *Elife* **7** (2018).

56 Zheng, S. Q. *et al.* MotionCor2: anisotropic correction of beam-induced motion for improved cryo-electron microscopy. *Nat Methods* **14**, 331-332 (2017).

57 Rohou, A. & Grigorieff, N. CTFFIND4: Fast and accurate defocus estimation from electron micrographs. *J Struct Biol* **192**, 216-221 (2015).

58 Bepler, T. *et al.* Positive-unlabeled convolutional neural networks for particle picking in cryo-electron micrographs. *Nat Methods* **16**, 1153-1160 (2019).
59 Rosenthal, P. B. & Henderson, R. Optimal determination of particle orientation, absolute hand, and contrast loss in single-particle electron cryomicroscopy. *J Mol Biol* **333**, 721-745 (2003).
60 Emsley, P., Lohkamp, B., Scott, W. G. & Cowtan, K. Features and development of Coot. *Acta Crystallogr D Biol Crystallogr* **66**, 486-501 (2010).
61 Pettersen, E. F. *et al.* UCSF Chimera--a visualization system for exploratory research and analysis. *J Comput Chem* **25**, 1605-1612 (2004).
62 Adams, P. D. *et al.* PHENIX: a comprehensive Python-based system for macromolecular structure solution. *Acta Crystallogr D Biol Crystallogr* **66**, 213-221 (2010).
63 Goddard, T. D. *et al.* UCSF ChimeraX: Meeting modern challenges in visualization and analysis. *Protein Sci* **27**, 14-25 (2018).
64 DeLano, W. L. The PyMOL molecular graphics system. (2002).
65 Guillerez, J., Lopez, P. J., Proux, F., Launay, H. & Dreyfus, M. A mutation in T7 RNA polymerase that facilitates promoter clearance. *Proc Natl Acad Sci U S A* **102**, 5958-5963 (2005).
66 Wang, Y., Yesselman, J. D., Zhang, Q., Kang, M. & Feigon, J. Structural conservation in the template/pseudoknot domain of vertebrate telomerase RNA from teleost fish to human. *Proc Natl Acad Sci U S A* **113**, E5125-5134 (2016).
67 Latrick, C. M. & Cech, T. R. POT1-TPP1 enhances telomerase processivity by slowing primer dissociation and aiding translocation. *EMBO J* **29**, 924-933 (2010).
68 Jansson, L. I. *et al.* Telomere DNA G-quadruplex folding within actively extending human telomerase. *Proc Natl Acad Sci U S A* **116**, 9350-9359 (2019).
69 Leontis, N. B., Stombaugh, J. & Westhof, E. The non-Watson-Crick base pairs and their associated isostericity matrices. *Nucleic Acids Res* **30**, 3497-3531 (2002).
70 Robert, X. & Gouet, P. Deciphering key features in protein structures with the new ENDscript server. *Nucleic Acids Res* **42**, W320-324 (2014).
71 Tummala, H. *et al.* Homozygous OB-fold variants in telomere protein TPP1 are associated with dyskeratosis congenita-like phenotypes. *Blood* **132**, 1349-1353 (2018).
72 Hoffman, T. W. *et al.* Pulmonary fibrosis linked to variants in the ACD gene, encoding the telomere protein TPP1. *Eur Respir J* **54** (2019).

Acknowledgments:

Funding: This work was supported by grants from NIH R35GM131901 and NSF MCB2016540 to J.F. and NIH R01GM071940 to Z.H.Z.. We acknowledge use of instruments at the Electron Imaging Center for Nanomachines supported by UCLA and instrumentation grants from NIH (1S10RR23057, 1S10OD018111 and U24GM116792) and NSF (DBI-1338135 and DMR-1548924).

Author contributions: B.L. prepared telomerase samples and performed telomerase activity assays and analysis; Y.H. performed cryo-EM data collection; Y.H. and B.L. processed cryo-EM data and built atomic models; Y.W. assisted with modeling; H.S. analyzed disease mutations;

Z.H.Z. supervised cryo-EM data collection and processing; J.F. supervised all aspects of the project; all authors contributed to figure and table preparation and to manuscript writing and editing.

Competing interests: Authors declare that they have no competing interests.

Data and materials availability: Cryo-EM density maps have been deposited in the Electron Microscopy Data Bank under accession numbers EMD-26085 (H/ACA RNP), EMD-26086 (Catalytic core combined), EMD-26087 (Catalytic core with TPP1), EMD-26096 (Catalytic core without TPP1), EMD-26088 (Catalytic core with H2A-H2B), EMD-26090 (Catalytic core with TPP1, P2a State 1-1), EMD-26091 (Catalytic core with TPP1, P2a State 1-2), EMD-26092 (Catalytic core with TPP1, P2a State 1-3), EMD-26093 (Catalytic core with TPP1, P2a State 2), EMD-26094 (Catalytic core without TPP1, P2a State 1) and EMD-26095 (Catalytic core without TPP1, P2a State 2). The atomic models have been deposited in the Protein Data Bank under accession codes 7TRC (H/ACA RNP), 7TRD (Catalytic core combined), 7TRE (Catalytic core with TPP1) and 7TRF (Catalytic core with H2A-H2B). The initial model for 3D reconstruction was retrieved from the EMDB with accession code EMD-7521. Other structures used in this study were retrieved from the PDB with accession codes 2I46 (TPP1 OB), 7LMA (*Tetrahymena* telomerase), 7BG9 (Human telomerase catalytic core), 7BGB (Human telomerase H/ACA RNP), and 5CQG (Tribolium TERT-like protein with inhibitor). Uncropped version of all the gels are included as Supplementary Fig. 1. Any other relevant data are available from the corresponding authors upon reasonable request.

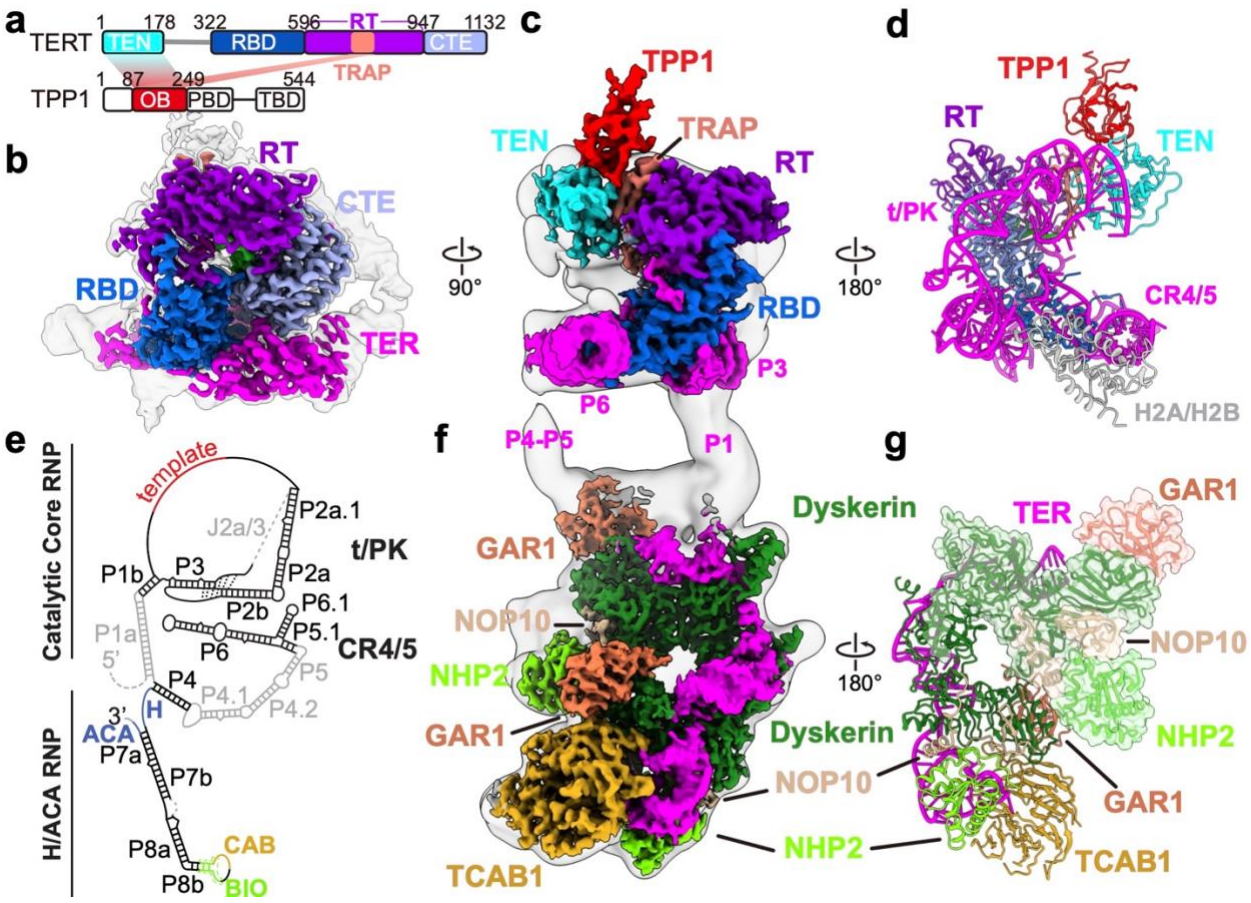

Fig. 1: Structure of human telomerase with TPP1. a, Schematic of TERT and TPP1 domains and interactions. OB, oligonucleotide/oligosaccharide-binding fold domain; PBD, POT1 binding domain; TBD, TIN2 binding domain. **b**, Cryo-EM density map of catalytic core at 3.3 Å resolution shown at two different thresholds. The high-threshold map showing high-resolution features is colored as in **a** for TERT and magenta for TER, and the low-threshold map showing the continuous density is overlayed as transparent surface. **c**, 3.5 Å resolution map of the catalytic core bound with TPP1. **d,** Cartoon model of the catalytic core. **e**, Schematic of TER secondary structure determined in the model. Regions invisible in the cryo-EM map are gray. **f**, **g**, Cryo-EM density map (**f**) and cartoon model (**g**) of H/ACA RNP. Cryo-EM map of the entire telomerase is shown behind (**c**) and (**f**).

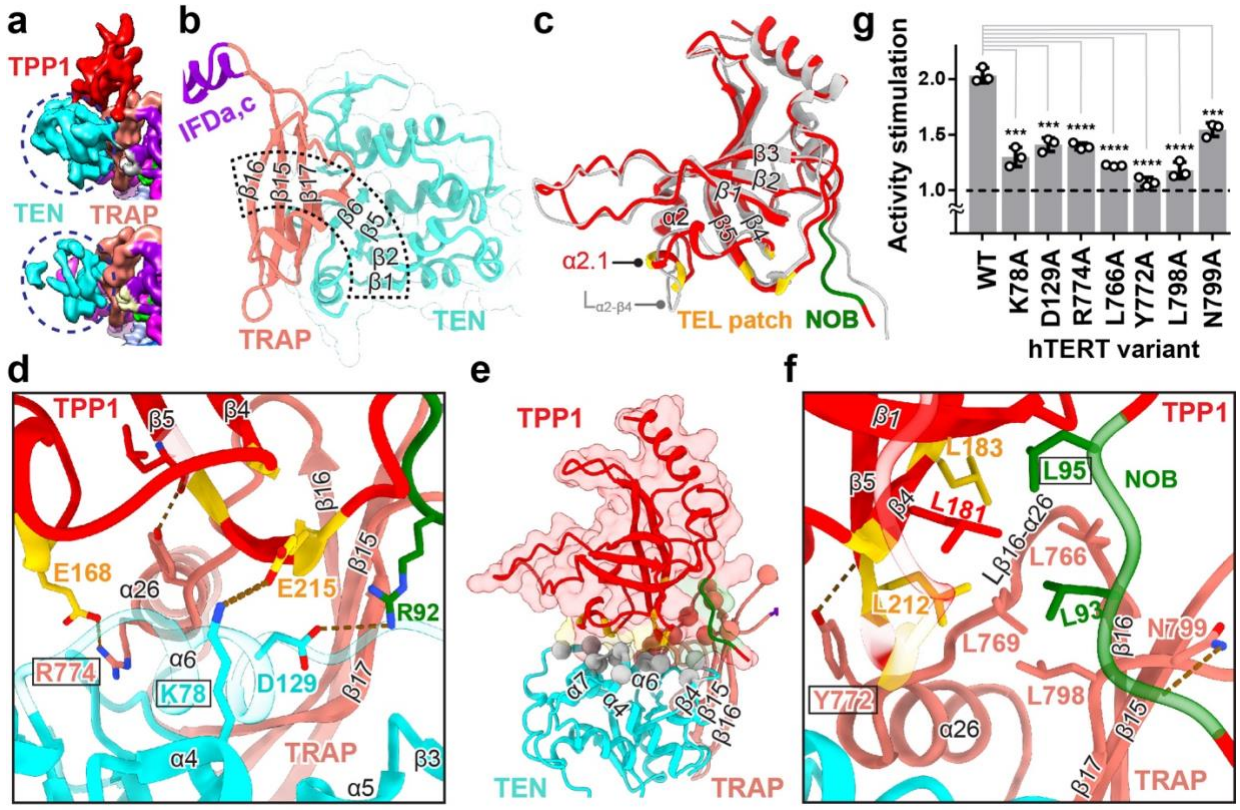

Fig. 2: TPP1 interactions with TERT TEN–TRAP. a, Cryo-EM maps of catalytic core with (top) and without (bottom) TPP1. Both maps are low-pass filtered to 5 Å for comparison. **b,** Structure of TEN–TRAP with the extended β sheet highlighted. **c,** Comparison of TPP1 structures in apo (gray) (PDB: 2I46) and telomerase-bound form (red). NOB and TEL patch residues are in green and yellow, respectively. **d-f**, TPP1 interface with TEN–TRAP. In **e,** TPP1 (red) sits on the top of TEN (cyan) and TRAP (salmon), with residues within 4 Å of the interface shown as spheres. Zoomed-in panels show the polar (**d**) and hydrophobic (**f**) interactions. Boxed residues are positions with disease mutations. **g,** Effect of TERT residue substitutions on telomerase activity stimulation by TPP1. Activity stimulation = activity with TPP1 / activity without TPP1. Plotted values are mean ± s.d. from n = 3 biologically independent experiments. ***, $p < 0.001$; ****, $p < 0.0001$; one-tailed unpaired t-tests.

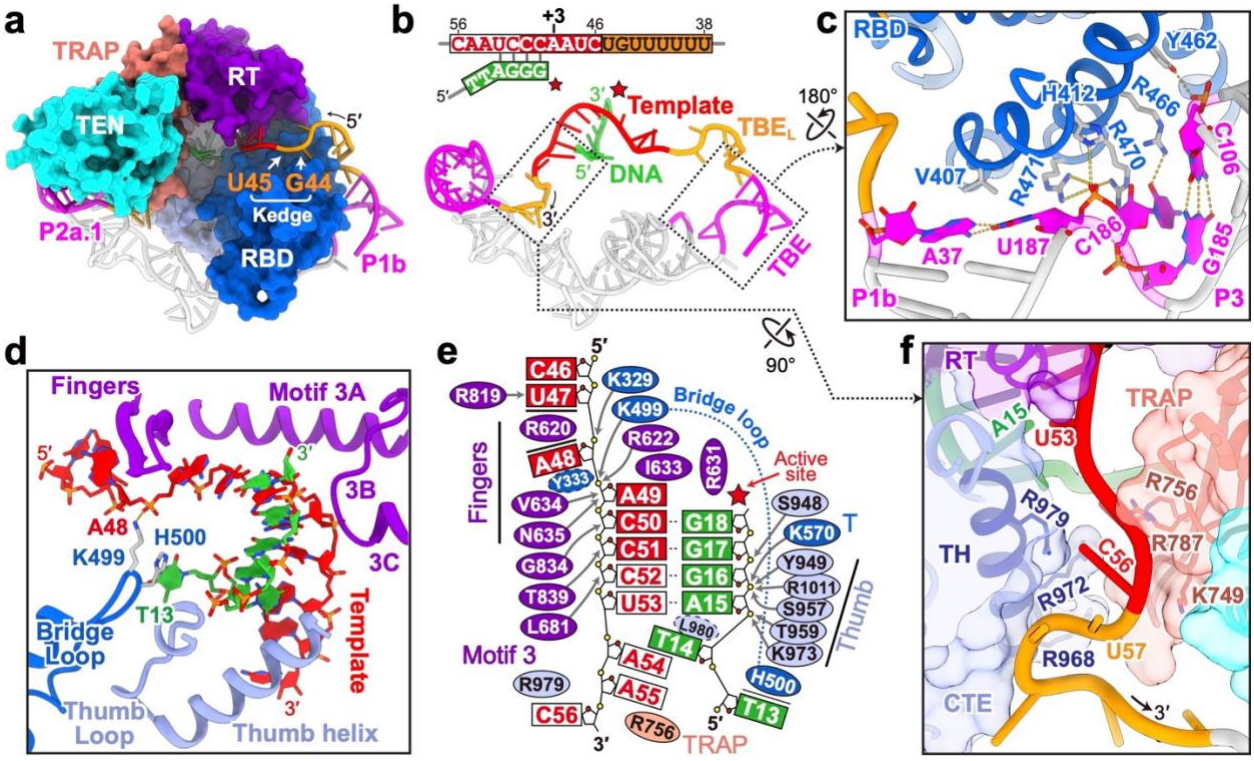

Fig. 3: Interactions between TERT and template–DNA duplex. a, b, The catalytic cavity of TERT (colored surface) with TER t/PK (gray ribbon) and DNA (green ribbon). TERT is omitted in **b** to show the template–DNA duplex. The template and adjacent single-stranded regions are colored red and orange, respectively. At top, template alignment nucleotides are red with a white background. P1b and P2a.1 are magenta. Red star represents the TERT active site. **c,** Detailed TERT–TER interactions in the region on the 5′-side of the template. **d,** Ribbon depictions of template–DNA and TERT motifs involved in duplex handling. Bridge loop K499 and H500 are shown as sticks. **e,** Schematic showing specific interactions between TERT and template–DNA duplex. Polar and stacking interactions are indicated with arrows and bold lines, respectively. **f,** The path of TER nucleotides on the 3′ side of the template. Positively charged TERT residues along the template exit path are shown as sticks.

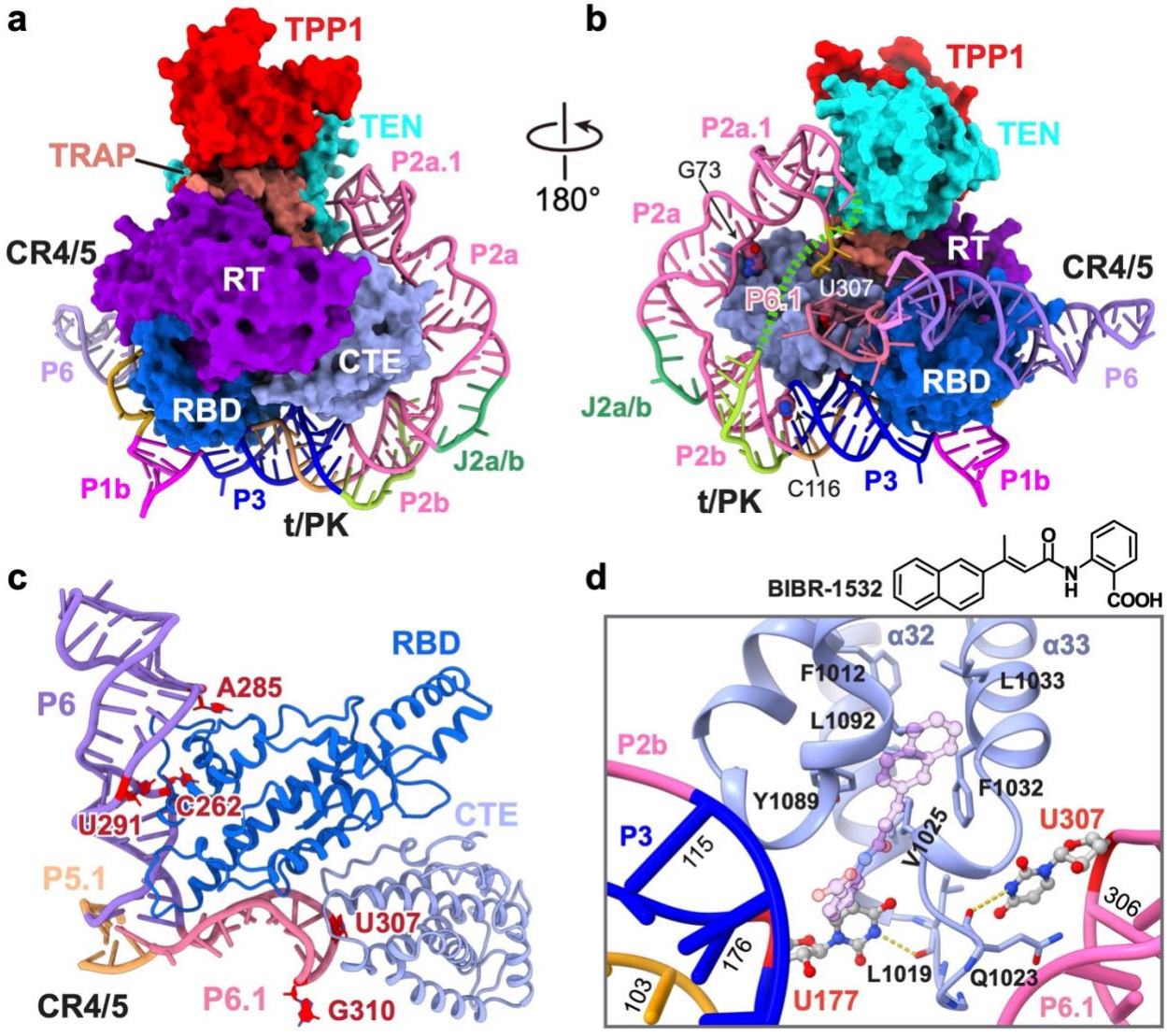

Fig. 4: Interactions between TERT and TER. a, b, Telomerase catalytic core structure shown in two views. View in **a** is same as Fig. 1b. The invisible linker between P2a.1 and P2b loop is shown as green dashed line in **b**. **c**, Structure of CR4/5 and its interactions with TERT RBD and CTE. Flipped out nucleotides (red) on P6 and P6.1 that interact with RBD and CTE, respectively, are labeled. G_{310} interacts with H2A/H2B. **d,** Interactions of U_{177} (PK) and U_{307} (CR4/5) with CTE $L_{\alpha32\text{-}\alpha33}$ residues L1019 and Q1023, respectively. Telomerase specific inhibitor BIBR1532 (light purple) is shown docked onto this structure based on the *Tribolium castaneum* TERT-like protein CTE–BIBR1532 structure (PDB: 5CQG). Residues comprising the 'FVYL' pocket for BIBR1532 binding[11] are labeled. BIBR1532 chemical structure is shown above.

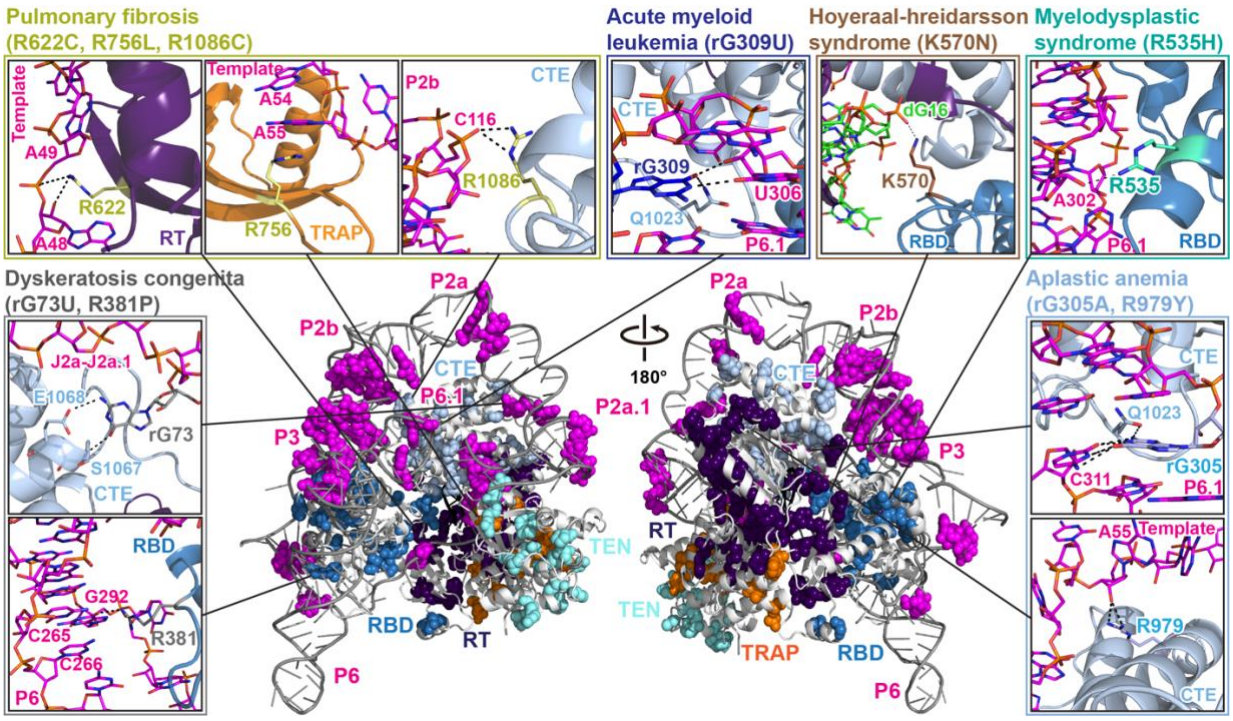

Fig. 5: Disease-associated mutations of human TERT and TER. (center) Cartoon representation of human TERT and TER (in gray) with mutations that are associated with disease (Supplementary Table 1[13]) highlighted as spheres and colored by their domains (colored as in Fig. 1). (clockwise from lower left) Close-up views of wild-type interactions in regions harboring some mutations causing various diseases.

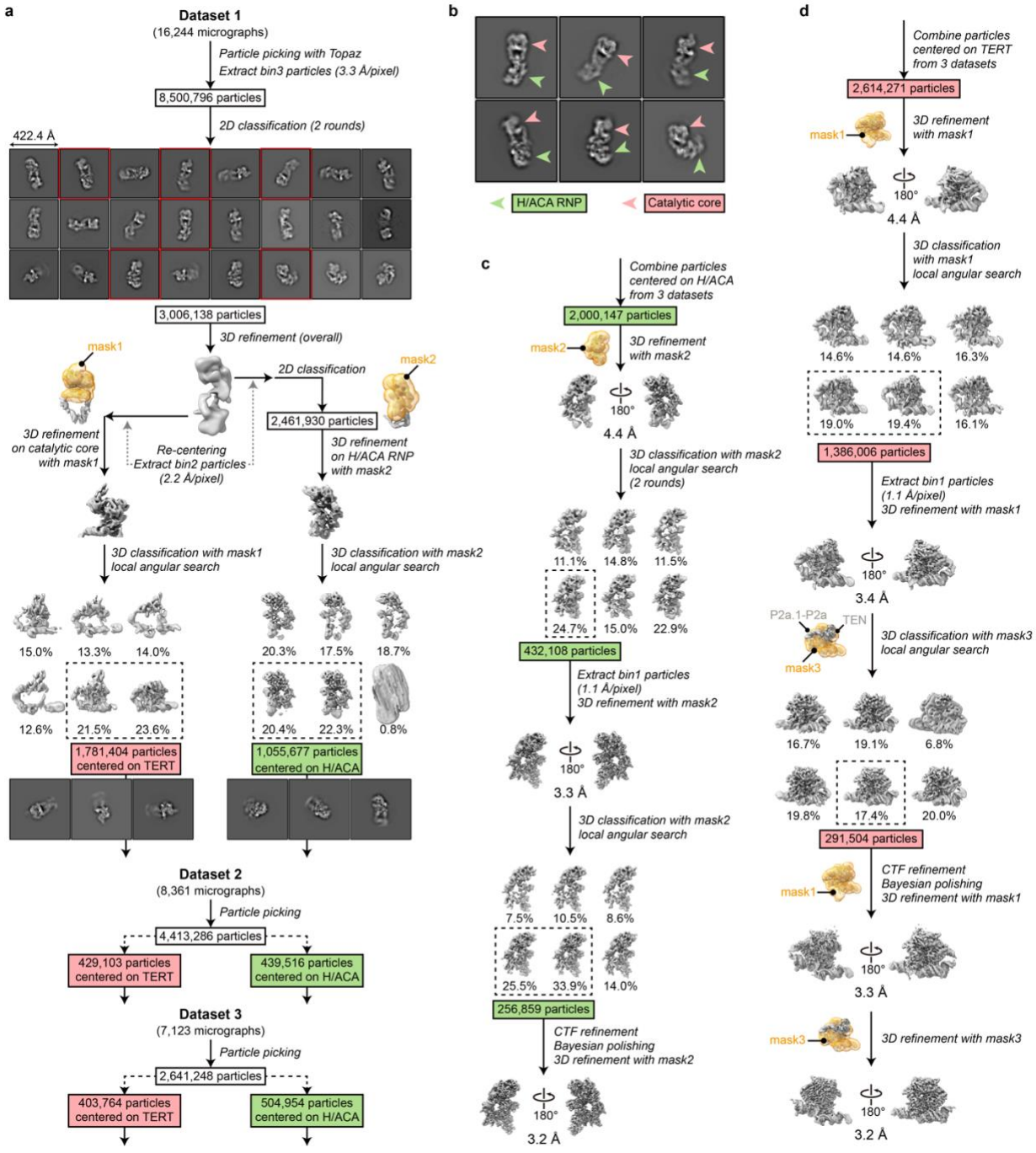

Extended Data Fig. 1: Cryo-EM data processing workflow of human telomerase (detailed in Methods). a, Initial screening of sub-particles centered on the catalytic core and H/ACA RNP. **b,** Representative 2D class images of human telomerase as indicated in the red boxes in **a**. **c, d,** 3D classification and reconstruction processes for the H/ACA RNP (**c**) and catalytic core (**d**). Soft masks used in the data processing are shown in orange.

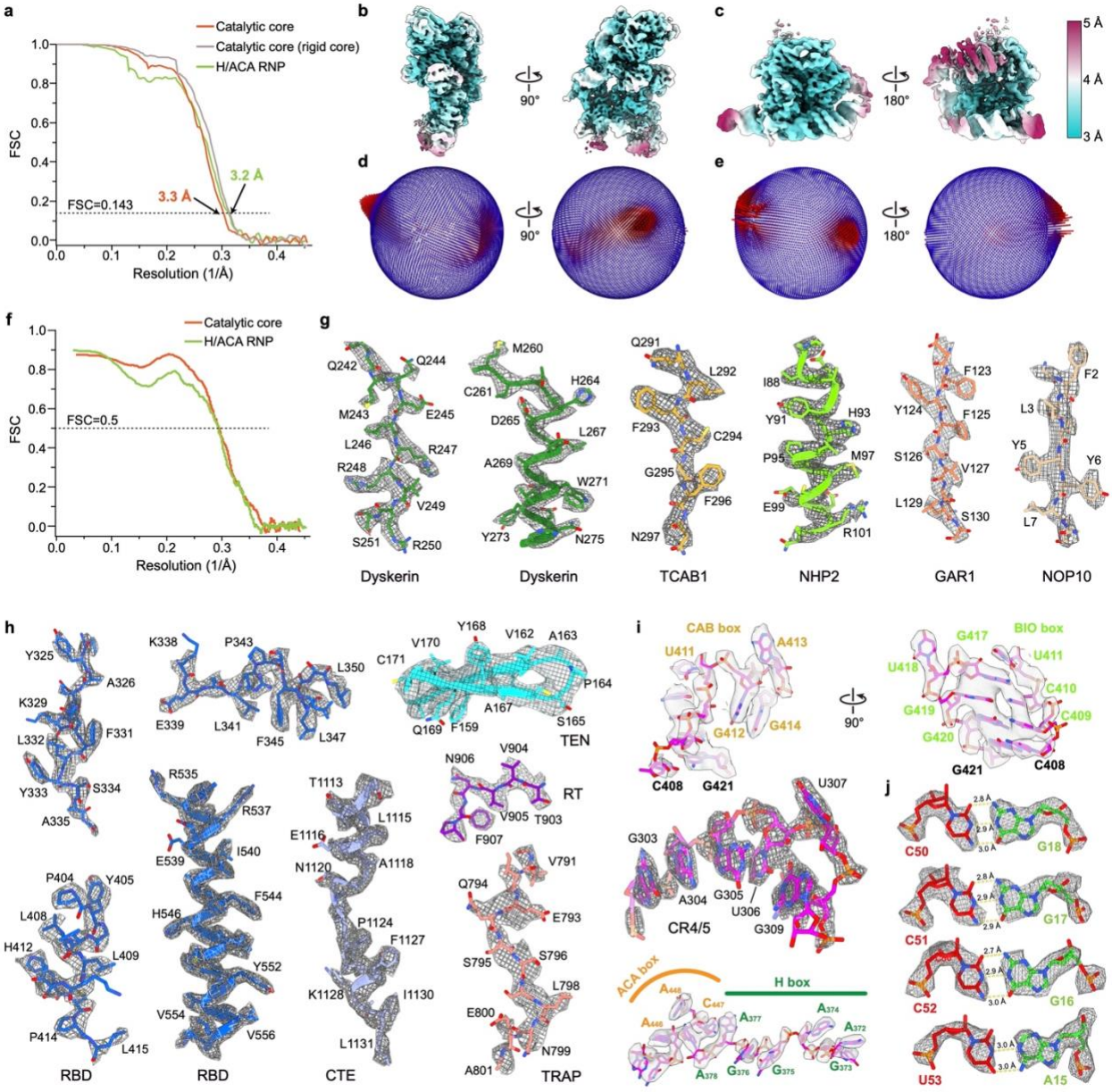

Extended Data Fig. 2: Evaluation of cryo-EM reconstructions. a, Plot of the Fourier shell correlation (FSC) as a function of the spatial frequency of the final reconstructions. **b, c,** Local resolution evaluation of the H/ACA RNP (**b**) and catalytic core (**c**) reconstructions. **d, e,** Euler angle distribution of sub-particles used for the H/ACA RNP (**d**) and catalytic core (**e**) reconstructions**. f,** FSC coefficients as a function of spatial frequency between model and corresponding cryo-EM density maps. **g-j,** Representative cryo-EM densities encasing the corresponding atomic models of H/ACA proteins (**g**), TERT (**h**), TER (**i**) and the four base pairs in the template–DNA duplex (**j**).

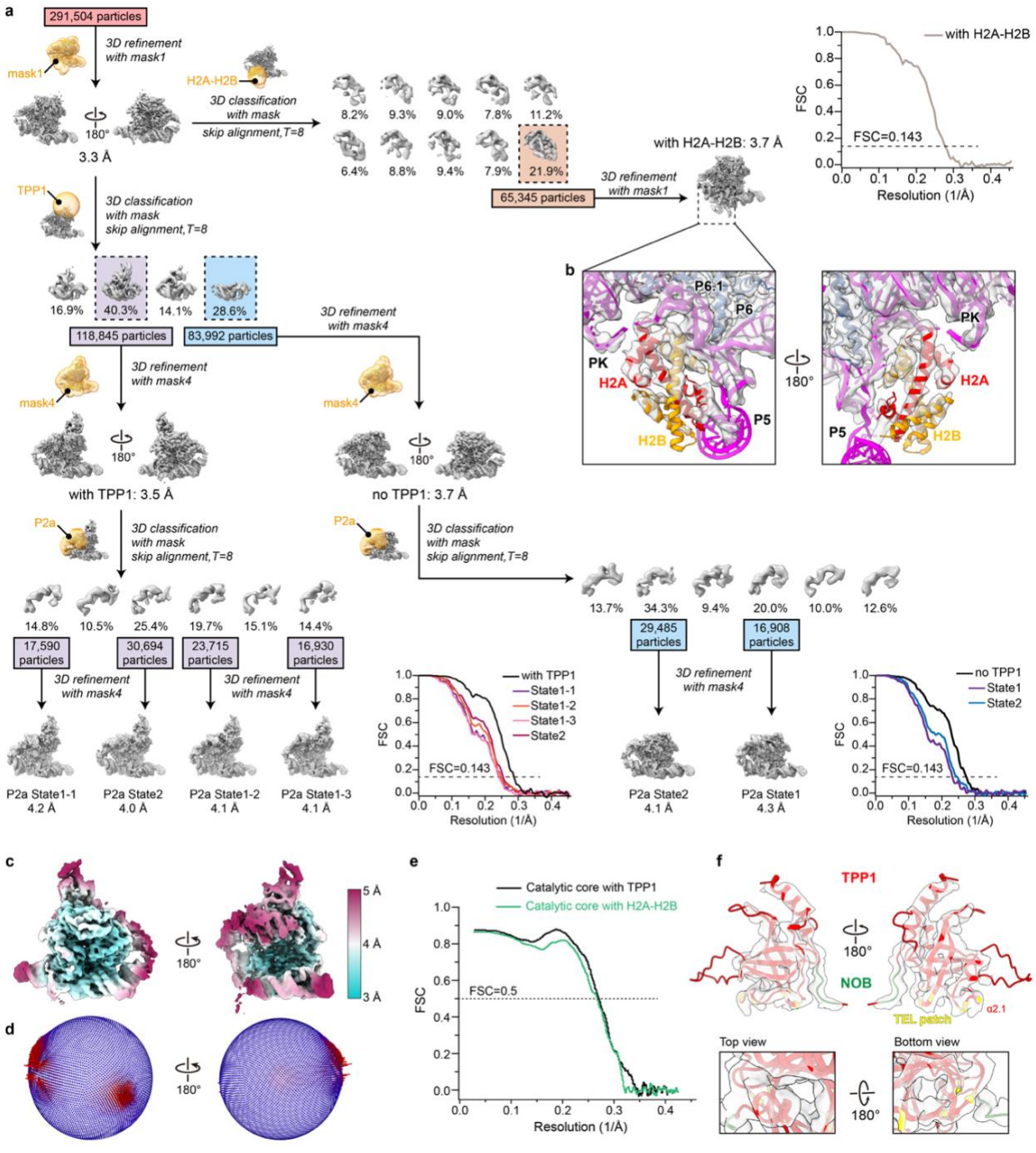

Extended Data Fig. 3: Analysis of compositional and conformational heterogeneity of the catalytic core. a, Cryo-EM 3D classification and reconstruction workflow with different masks. Insets show the FSC curves of final reconstructions. **b,** Superposition of H2A-H2B model and cryo-EM density. **c,** Local resolution evaluation of the 3.5 Å resolution reconstruction of catalytic core bond with TPP1. **d,** Euler angle distribution of sub-particles used for the reconstruction of catalytic core bound with TPP1. **e,** Model VS map FSC curve of the reconstruction with TPP1 or H2A-H2B. **f,** Superposition of TPP1 model and cryo-EM density.

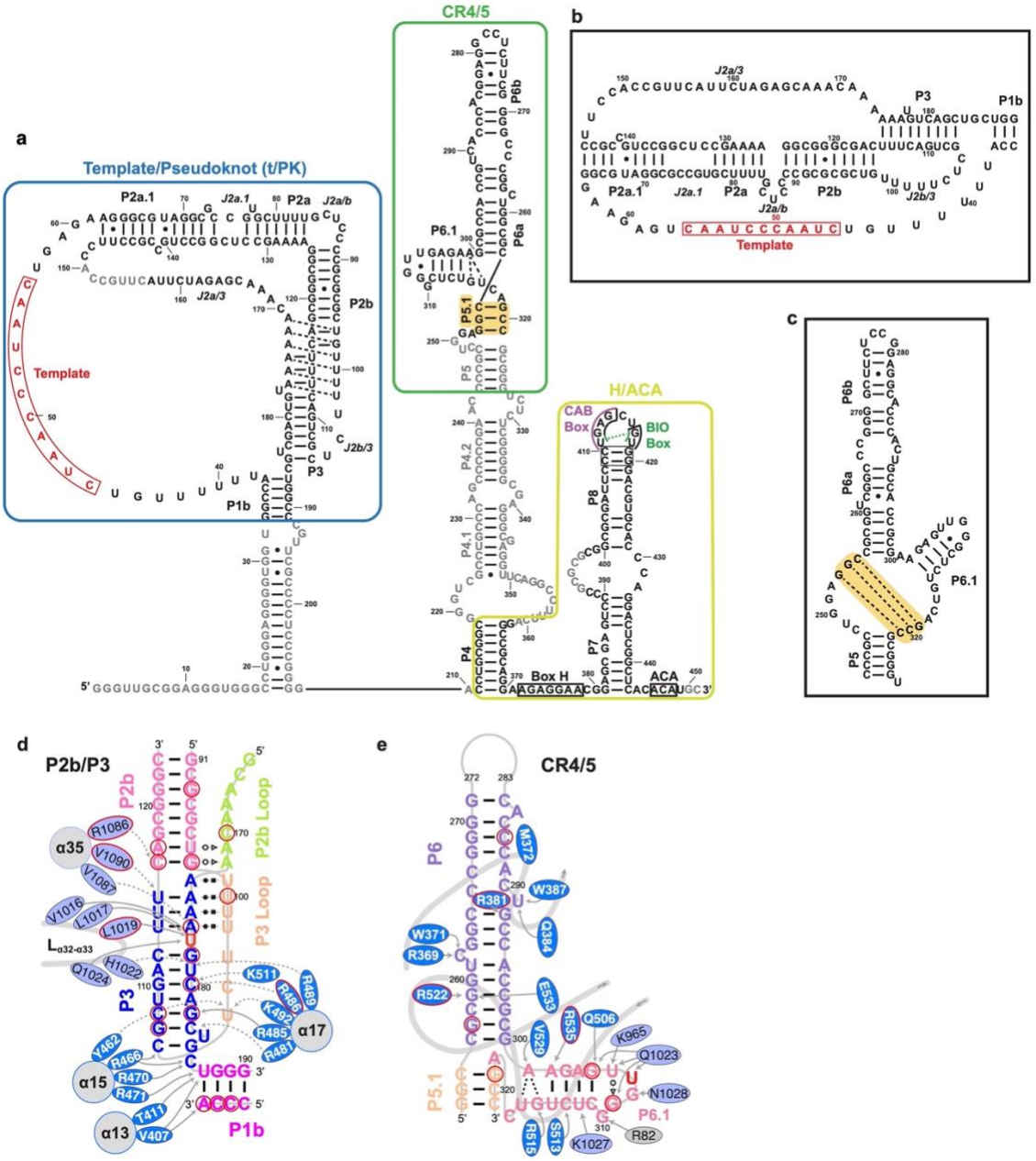

Extended Data Fig. 4: Secondary structure of human TER and interactions with TERT. a, Secondary structure observed in our telomerase structure (black), with unmodeled regions (gray) based on the telomerase database[13]. **b, c,** The previously predicted secondary structures of t/PK (**b**) and CR4/5 (**c**) based on phylogenetic analysis[13]. The dashed lines connecting residues in **c** indicate interactions forming the 3 bp P5.1 (highlighted) found in our structure, added for clarity. **d**, **e**, Structure-based schematics of TER P2b/P3-P1b (**d**) and CR4/5 (**e**) and interactions with TERT. Solid and dashed arrows from TERT residues to TER nucleotides indicate interactions with base and backbone, respectively. Base pair types are indicated using Leontis-Westhof symbols[69]. Red circles/ovals indicate residue positions with disease related mutations.

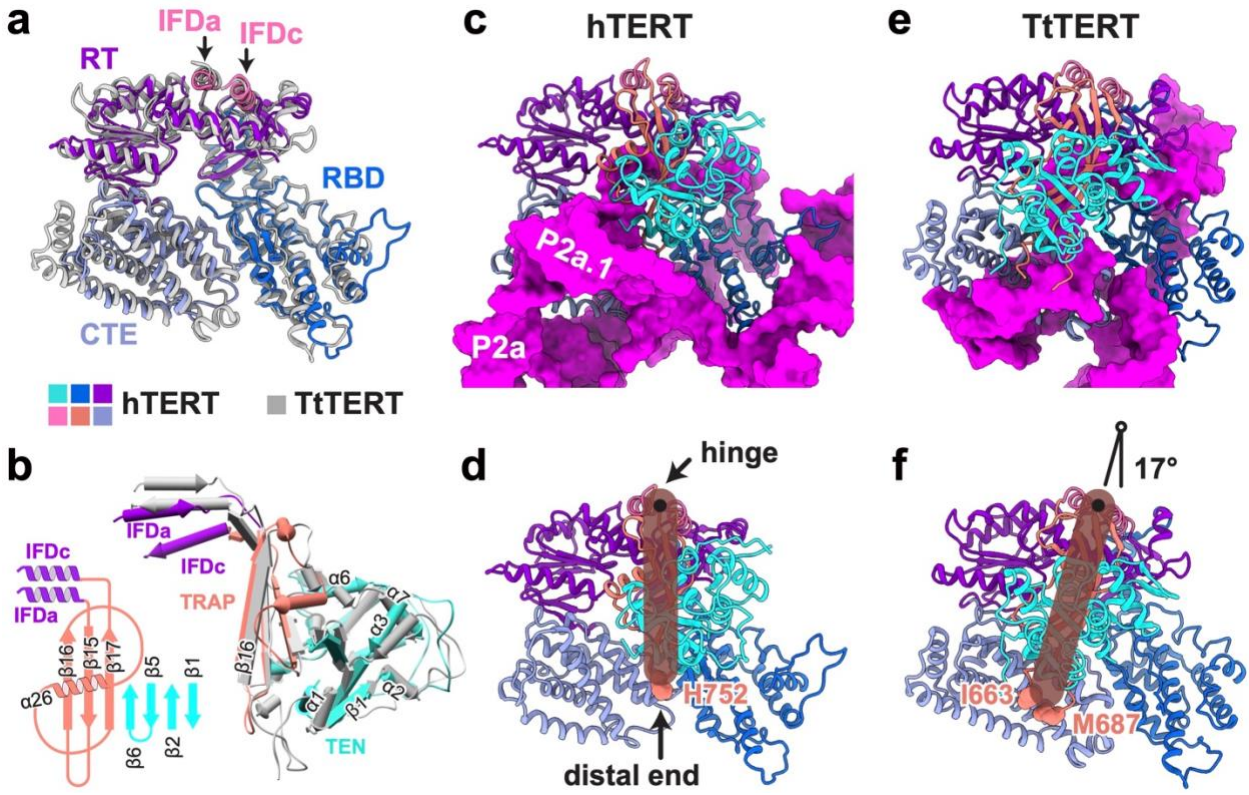

Extended Data Fig. 5: Comparison of human and *Tetrahymena* TERT structure. a, Superposition of RBD–RT–CTE ring (TERT ring) structures of hTERT and *Tetrahymena* TERT (TtTERT, PDB: 7LMA). **b,** Overlay of TEN–IFD-TRAP structures in human (colored) and *Tetrahymena* (gray) telomerase. Inset shows the secondary structure of human TRAP and the extended β sheet between TEN and TRAP. **c-f,** Comparison of human and *Tetrahymena* TEN–TRAP position relative to the TERT ring. Ribbon diagrams of the TERT rings from hTERT (**c-d**) and TtTERT (**e-f**) are shown in the same orientations as in A. Human and *Tetrahymena* TER are shown as magenta surfaces in **c** and **e**, respectively. Transparent sticks in **d** and **f** indicate the orientations of TRAP domains in hTERT and TtTERT, respectively. Residues located at the distal end of TRAP domains are shown as spheres. The hinge of the "rotation movement" is at the proximal end of TRAP that is connected to the IFDa and IFDc helices.

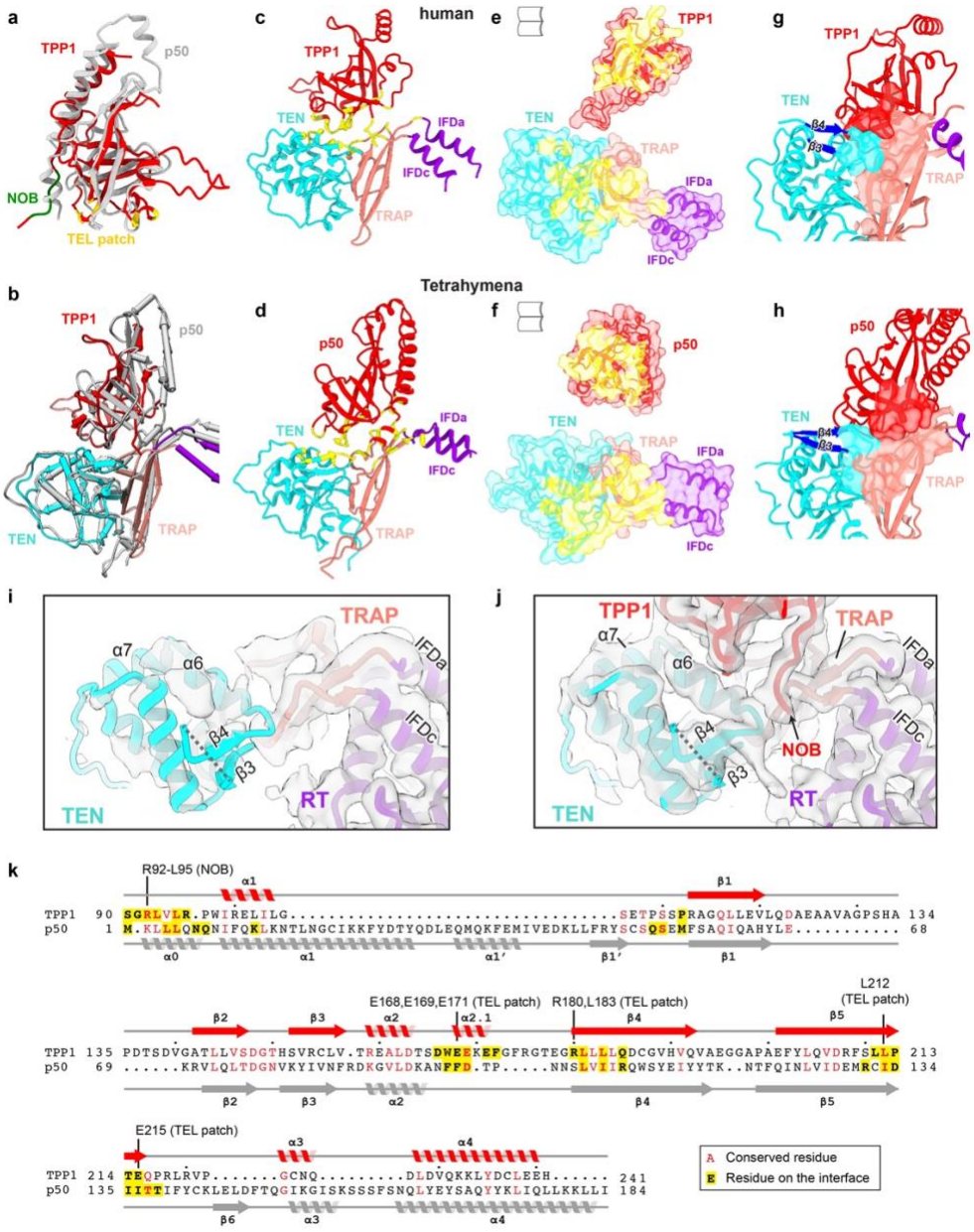

Extended Data Fig. 6: Comparison of human TEN–TRAP–TPP1 and *Tetrahymena* TEN–TRAP–p50. a, Comparison of telomerase-bound TPP1 and p50 (gray) (PDB: 7LMA). **b,** Superposition of human TEN–TRAP–TPP1 (colored as in Fig. 2) and *Tetrahymena* TEN–TRAP–p50 (gray). **c, d,** Overall comparison of human TEN–TRAP–TPP1 (**c**) and *Tetrahymena* TEN–TRAP–p50 (**d**) with the residues locate on the interfaces colored yellow. **e, f,** Open book views of the continuous interfaces between human TPP1–TERT (**e**) and *Tetrahymena* p50–TERT (**f**) shown as surface, respectively. **g, h,** A three-way junction shared by human TEN–TRAP–TPP1 (**g**) and *Tetrahymena* TEN–TRAP–p50[10] (**h**). **i, j,** Density maps of TEN and TRAP without (**i**) and with (**j**) TPP1, highlighting the changes in density upon TPP1 binding. Density thresholds were adjusted for comparable density in the RT region. **k,** Structure-based sequence alignment (rendered with ESPript3[70]) for human TPP1 (red) and *Tetrahymena* p50 (grey). Residues located on the interface are highlighted in yellow. Residues comprising TPP1 NOB and TEL patch are indicated on the top of alignment.

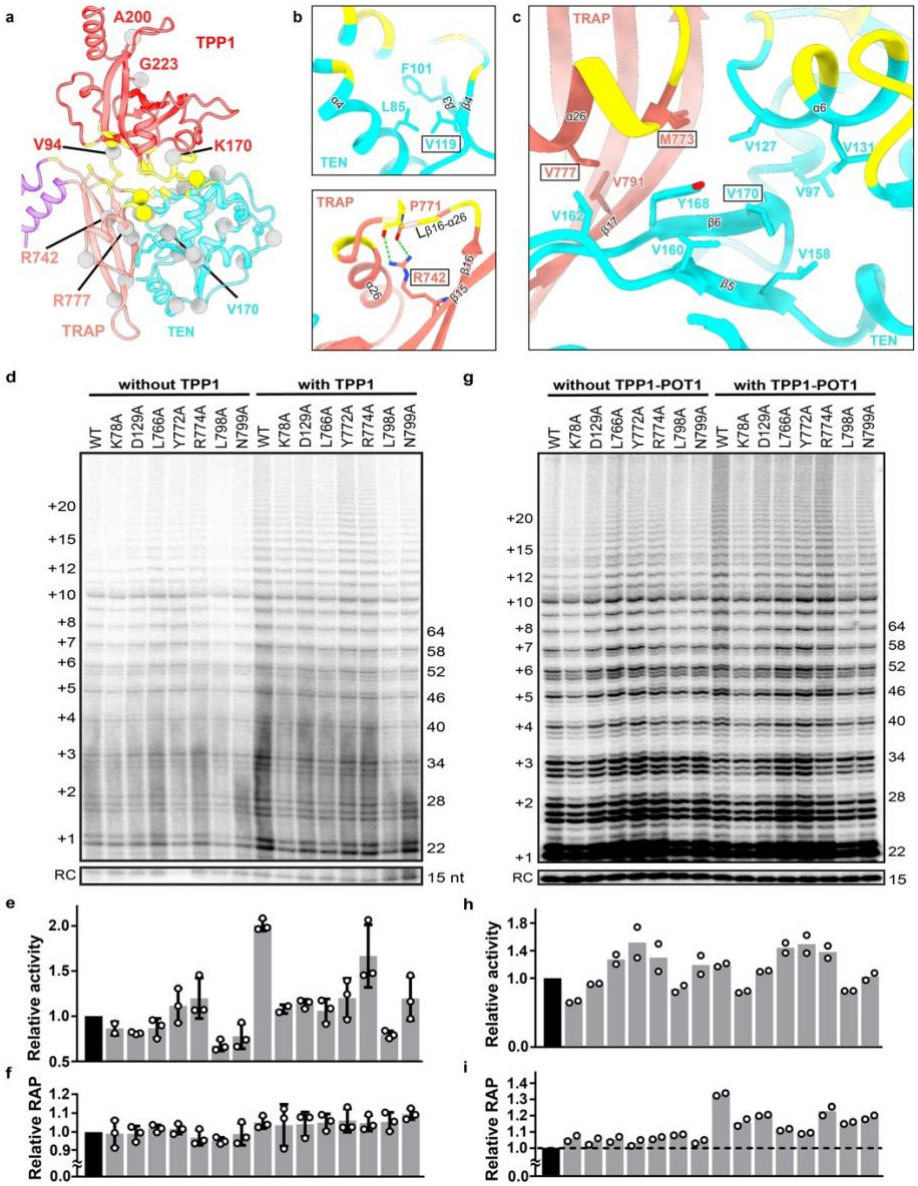

Extended Data Fig. 7: Disease related mutations and telomerase activity assays. a-e Locations of disease related mutations. **a,** Back view of TEN–TRAP–TPP1 interface as in Extended Data Fig. 6. Residue positions with disease mutations in TEN, TRAP, and TPP1 (Supplementary Table 1[13,71,72]) are shown as yellow (interface) and gray (non-interface) spheres. **b, c,** Zoomed-in views of intra-(**b**) and inter-(**c**) domain interactions from residues related to disease mutations that may disrupt TPP1–TERT interaction indirectly. **d-i** Telomerase activity assays for TERT variants with residue substitutions at the interface with TPP1. **d,** Telomerase activity assays corresponding to Fig. 2g. Gel is a representative from 3 independent experiments. The number of telomeric repeats added to primer are indicated at left, and number of nucleotides are indicated at right. RC, recovery control. **e, f,** Relative activity (**e**) and RAP (**f**) normalized to TERT WT without TPP1. Plotted values are mean ± s.d. from n = 3 biologically independent experiments. **g**, Telomerase activity assays without and with TPP1–POT1. Gel is a representative from 2 independent experiments. **h, i,** Relative activity (**h**) and RAP (**i**) normalized to TERT WT without TPP1-POT1. Open circles are values from n = 2 biologically independent experiments.

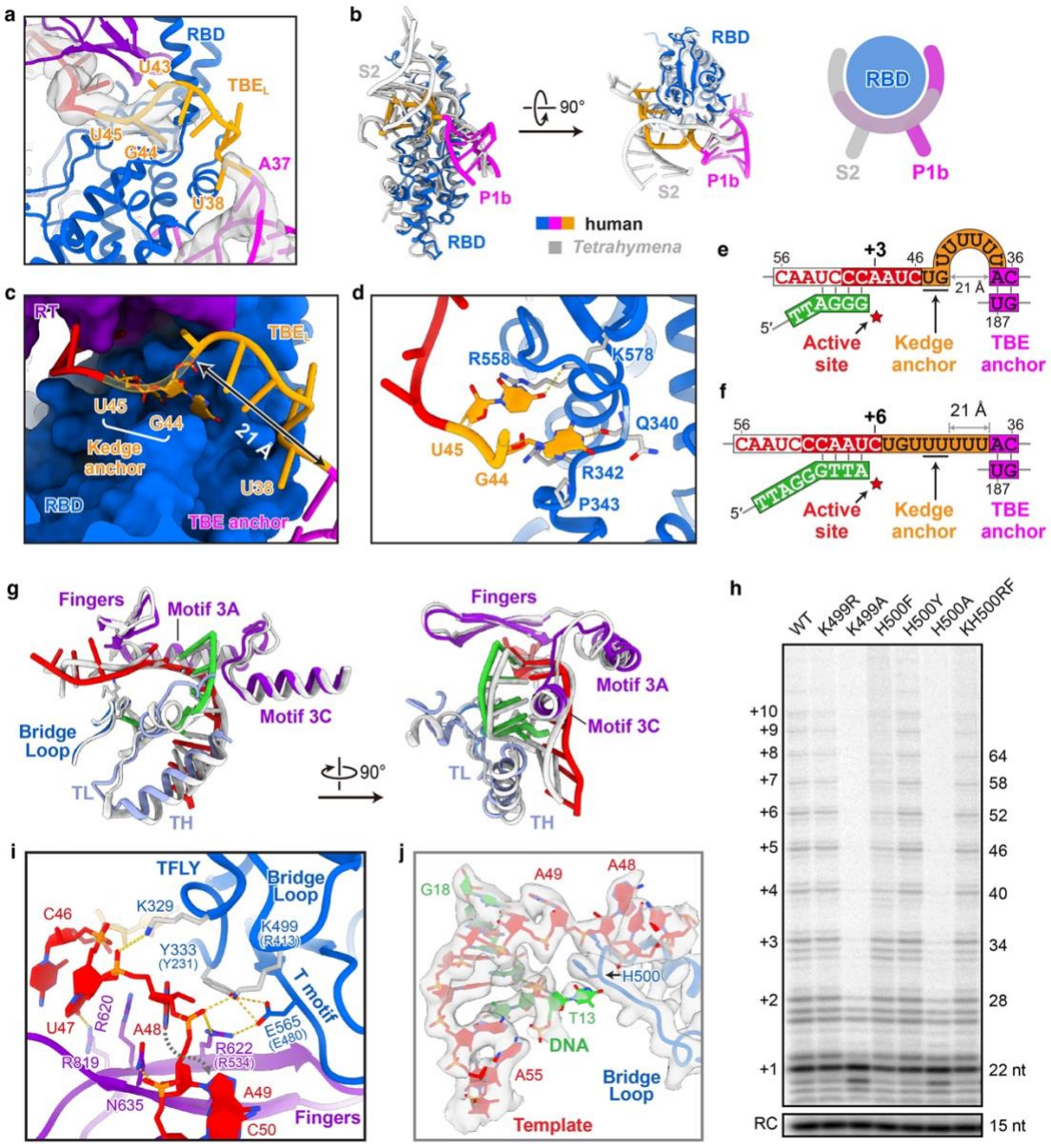

Extended Data Fig. 8: Structural details of the TBE, bridge loop and related activity assays. a, Structure of the single-stranded RNA nucleotides at the 5′ side of the template in complex with TERT RBD (colored as in Fig. 3a). Cryo-EM densities of TER nucleotides are overlayed on the structure as transparent surfaces. Only the first two template-adjacent nucleotides ($G_{44}U_{45}$) and P1b have strong densities in the cryo-EM map, whereas the intervening nucleotides show only weak density indicative of positional dynamics. **b,** Comparison of the TBE-TBE$_L$-RBD structures from human (color) and *Tetrahymena* (gray, PDB: 7LMA) telomerase. **c,** G_{44} and U_{45} in the kedge anchor pocket of TERT RBD. The linear distance from the phosphate group of U_{38} to the phosphate group of G_{44} is about 21 Å. **d,** Detailed interactions between G_{44}-U_{45} and TERT RBD. Intermolecular hydrogen bonds are shown as dashed yellow lines. **e,** Schematic of TER TBE-TBE$_L$-template conformation when the template is at the +3 position as in our structure. **f,** Predicted TBE-TBE$_L$-template conformation

when the template is at the +6 position. TBE_L nucleotides $U_{38\text{-}40}$ would be fully stretched to span the distance (21 Å) from the TBE anchor to the kedge anchor. **g,** Comparison of the template–DNA duplex and surrounding structural elements of human (color) and *Tetrahymena* (gray, PDB: 7LMA) telomerase. Residues located on the tip of the bridge loop are shown as sticks. **h,** Telomerase activity assays with substitutions of hTERT K499 and/or H500. Gel is a representative from 2 independent experiments. **i,** Detailed interactions surrounding the entrance of template nucleotides. Side chains of key residues are indicated with corresponding *Tetrahymena* TERT residues in parentheses. **j,** Ribbon diagram of the template-DNA duplex and the bridge loop superimposed with cryo-EM densities (transparent surface).

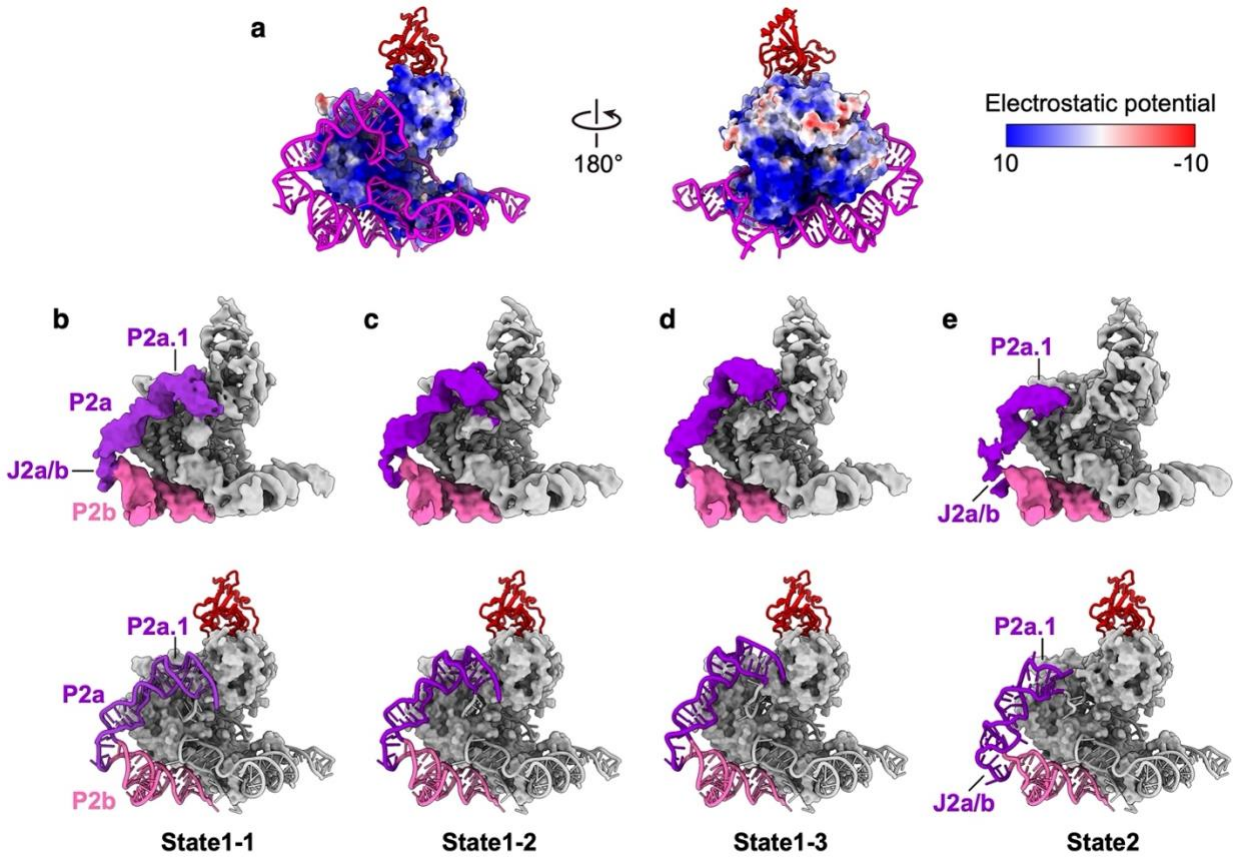

Extended Data Fig. 9: Electrostatic interactions and conformational dynamics of the pseudoknot on TERT. a, Electrostatic surface of TERT shown in two different views. **b-e,** Cryo-EM density (upper) and model (lower) of telomerase catalytic core with P2 stem in State1-1 (**b**), State1-2 (**c**), State1-3 (**d**) and State2 (**e**). Through State1-1 to 1-3 (**b-d**), P2a.1 conducts an upward movement. From State1-1 (**b**) to State2 (**e**), P2a.1 and P2a move away from TEN domain of TERT with the J2a/b linker bulged out. The conformation of P2b and its location on TERT remain the same in the four structures.

Extended Data Table 1: Cryo-EM data collection, refinement and validation statistics for human telomerase maps and models.

	H/ACA RNP (EMD-26085) (PDB 7TRC)	Catalytic core combined (EMD-26086) (PDB 7TRD)	Catalytic core with TPP1 (EMD-26087) (PDB 7TRE)	Catalytic core without TPP1 (EMD-26096)	Catalytic core with H2A-H2B (EMD-26088) (PDB 7TRF)
Data collection and processing					
Magnification	81,000	81,000	81,000	81,000	81,000
Voltage (kV)	300	300	300	300	300
Electron exposure (e–/Å^2)	55	55	55	55	55
Defocus range (μm)	−0.8 – −4.0	−0.8 – −4.0	−0.8 – −4.0	−0.8 – −4.0	−0.8 – −4.0
Pixel size (Å)	1.1	1.1	1.1	1.1	1.1
Symmetry imposed	C1	C1	C1	C1	C1
Initial particle images (no.)	15,555,330	15,555,330	15,555,330	15,555,330	15,555,330
Final particle images (no.)	256,859	291,504	118,845	83,992	65,345
Map resolution (Å)	3.2	3.3	3.5	3.7	3.7
FSC threshold	0.143	0.143	0.143	0.143	0.143
Map resolution range (Å)	3.2–6.0	3.3–6.0	3.5–7.0	3.7–7.0	3.7–7.0
Refinement					
Initial model used (PDB code)	7BGB		2l46		7BG9
Model resolution (Å)	3.4	3.4	3.6		3.7
FSC threshold	0.5	0.5	0.5		0.5
Map sharpening *B* factor (Å^2)	−106.0	-100	-100		-50
Model composition					
Non-hydrogen atoms	14,747	12,240	13,411		13,581
Protein residues	1,599	934	1,086		1,106
RNA/DNA Nucleotides	92	224	224		224
Ligands	0	0	0		0
R.m.s. deviations					
Bond lengths (Å)	0.003	0.004	0.006		0.005
Bond angles (°)	0.645	0.622	0.757		0.734
Validation					
MolProbity score	1.74	1.71	1.82		1.73
Clashscore	8.21	7.37	7.28		7.36
Poor rotamers (%)	0.21	0.12	0.11		0.10
Ramachandran plot					
Favored (%)	95.80	95.67	93.58		95.33
Allowed (%)	4.20	4.33	6.42		4.58
Disallowed (%)	0.00	0.00	0.00		0.09

	Catalytic core with TPP1, P2a State1-1 (EMD-26090)	Catalytic core with TPP1, P2a State1-2 (EMD-26091)	Catalytic core with TPP1, P2a State1-3 (EMD-26092)	Catalytic core with TPP1, P2a State2 (EMD-26093)	Catalytic core without TPP1, P2a State1 (EMD-26094)	Catalytic core without TPP1, P2a State2 (EMD-26095)
Data collection and processing						
Magnification	81,000	81,000	81,000	81,000	81,000	81,000
Voltage (kV)	300	300	300	300	300	300
Electron exposure (e–/Å^2)	55	55	55	55	55	55
Defocus range (μm)	−0.8 – −4.0	−0.8 – −4.0	−0.8 – −4.0	−0.8 – −4.0	−0.8 – −4.0	−0.8 – −4.0
Pixel size (Å)	1.1	1.1	1.1	1.1	1.1	1.1
Symmetry imposed	C1	C1	C1	C1	C1	C1
Initial particle images (no.)	15,555,330	15,555,330	15,555,330	15,555,330	15,555,330	15,555,330
Final particle images (no.)	17,590	23,715	16,930	30,694	16,908	29,485
Map resolution (Å)	4.2	4.1	4.1	4.0	4.3	4.1
FSC threshold	0.143	0.143	0.143	0.143	0.143	0.143
Map resolution range (Å)	4.2–8.0	4.1–8.0	4.1–8.0	4.0–8.0	4.3–8.0	4.1–8.0